WE-NEED

WatEr NEEDs, availability, quality and sustainability

Deliverable Number:	D5.2
Work package number:	WP5
Deliverable title	REPORT ON THE APPLICATION OF THE RISK MODEL TO THE FIELD SITE
Type	Report
Dissemination Level	Public
Lead participant	Politecnico di Milano
Contributing scientists and other personnel	Polimi: Emanuela Bianchi Janetti, Aronne Dell'Oca, Alberto Guadagnini, Giovanni M. Porta, Martina Siena, Monica RivaUPC: Daniel Fernàndez-Garcia, Guillem Solé-Marí. UAVR:Susana Loureiro, Rui Morgado, Maria Pavlaki Weizmann: Brian Berkowitz, Ishai Dror.
Scheduled delivery date	20 July 2019
Actual / forecast delivery date	20 July 2019

Deliverable summary

We introduce, develop and test a Groundwater Probabilistic Risk Model, GPRM, aimed at assessing (and preventing) negative issues related to water resources management and exploitation. GPRM combines a wide range of data to promote improved governance of groundwater by balancing economic development, sustainability and social involvement and to increase certainty through quantification of risk. This document illustrates the implementation of GPRM for the two considered showcases (Cremona and Bologna aquifers) of WE-NEED. Relevant and practically-oriented scenarios identified with the support of the stakeholders have been analyzed. Different risk pathways are presented formally forming a fault tree model, which enables identification of all basic events contributing to the undesired system failure. The latter is quantified in terms of depletion of natural springs and contamination of pumping wells respectively for the Cremona and the Bologna aquifers.

D5.2

Report on the application of the risk model to the field sites

Contents

1. Introduction

Groundwater is at risk from a variety of causes, including over-abstraction and pollution. The Groundwater Probabilistic Risk Management Model, GPRM, is a modern, interdisciplinary approach aimed at assessing (and preventing) negative issues related to water resources management. The model combines a wide range of data to promote improved governance of groundwater by balancing economic development, sustainability and social involvement. Risks associated with the use of groundwater for supply or productive uses and resulting in the failure of the system, quantifiable in terms of depletion of natural springs and/or contamination of pumping wells, is treated considering a multidisciplinary approach, involving stakeholders. GPRM makes use of data taken for multiple entries of various origins and synthesizes them in a descriptive and simplified set of indicators, easily transferable to decision makers. Different risk pathways are presented formally forming a fault tree model, which enables identification of all basic events contributing to the undesired system failure. This allows reduction of the dimensionality of the parameter space, thus reducing a markedly complex problem into a set of manageable tasks (de Barros et al, 2011). Data and results of process identification from WPs 1-4 are treated and combined into a fault tree model as elemental components to ultimately assist decision makers in developing strategies to minimize risks to society and environment, as well as to allocate characterization efforts to reduce the overall uncertainty (associated with a given indicator metric) through data acquisition campaigns.

The focus of the application of the GPRM to the two field sites is different due to the diverse key features of the two aquifers. Considering the Bologna field, we study the hypothetical occurrence of groundwater contamination at the most important extraction wells or groups of wells addressed in Deliverable 2.3. In the Cremona field, we analyze the hypothetical depletion of natural high-quality water springs, which are the main supply to agriculture and a key environmental driver of the site. For this reason, the application of the GPRM to Cremona field site has be devoted to identify new sustainable groundwater management strategies for the protection and preservation of the natural springs environment. This Deliverable is structured as follows.

Section 2 provides a description of the application of GPRM at the Bologna pilot site. Transport model and probabilistic approach are described in Section 2.1. Results are embedded in Section 2.2. Section 3 focuses on the analysis of natural springs depletion at the Cremona pilot site. Description of the methodology is provided in Section 3.1 and 3.2. Section 3.3 describes the data set used. Section 3.4 illustrates the main results achieved. Section 4 summarizes the key conclusions of this work.

2. Bologna site

2.1 Transport model and probabilistic approach

The focus of the risk assessment at the Bologna site is the hypothetical occurrence of contaminants in the groundwater at sensitive locations, coinciding with the five most important extraction wells or groups of wells addressed in Deliverable 2.3. Here, a crucial part of the risk assessment is the quantification, within a probabilistic framework, of contaminant concentrations arriving at the extraction wells in the event that contaminants are introduced into the aquifer at the ground level. This step is feasible relying on the stochastic flow and transport models developed in Deliverable 2.2. Another important piece of information that is introduced into the risk assessment is the land use coverage, extracted from the Corine Land Cover (2012) as reported in Deliverable 2.2, and simplified to four land use categories as shown in Figure 2.1b: (1) Urban, (2) Industrial, (3) Agricultural and (4) Natural (i.e., absence of anthropic modification) land use. In the following, we explain how we couple this land use information with the flow and transport model results to obtain worst-case-scenario predictions of contamination at the extraction wells considering representative contaminants.

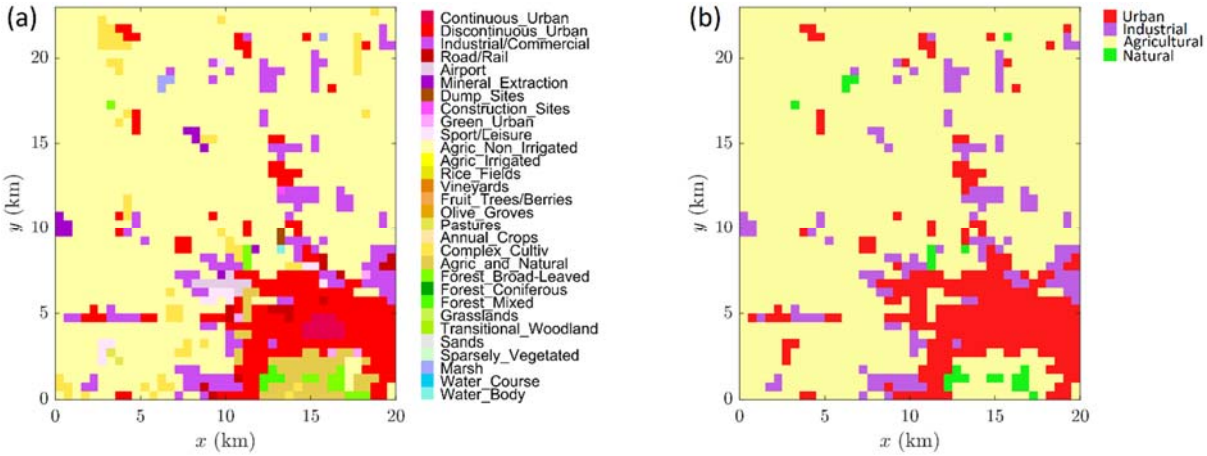

Figure 2.1. (a) Land use categorization extracted from the Corine Land Cover (2012) database, projected on the horizontal extension of the Bologna flow and transport model. (b) Simplified (four) land use categories.

In Deliverable 2.2 we analyze the (a) distributions of particle arrival times $T_{j,p}$, released from each well j in reverse-time simulation mode, to the aquifer top and (b) corresponding land use $\ell_{j,p}$ at the (reverse-time) arrival point. Each particle has an associated weight $w_{j,p}$ which represents its share of the total water flux to the well j. Through a few simplifying assumptions (which we list below), this information allows to evaluate concentration breakthrough curves at the wells.

We consider a continuous injection of a compound i (starting at initial time, $t = 0$) over the top of the aquifer in the area associated with a Land Use $\mathcal{L}_i$ (e.g., agricultural) with uniform input concentration C_i^0, and transported by advection and linear kinetic reaction. These assumptions give conservative estimates of risk in terms of risk assessment (upper bound of risk). The temporal dynamics of the concentration of contaminant i in the extracted water at well j can be determined as

$$C_{i,j}(t) = C_i^0 \sum_{p=1}^{N_j} w_{j,p}^* \, I\left(\ell_{j,p} = \mathcal{L}_i \,\&\, T_{j,p} \le t\right) \exp\left(-\lambda_i T_{j,p}\right), \qquad (2.1)$$

where $w_{j,p}^* = w_{j,p} / \sum_{q=1}^{N_j} w_{j,q}$, λ_i is the linear reaction coefficient associated with compound i, and $I(\mathrm{S})$ is an indicator function which is equal to 1 when the logical statement S is true, and 0 otherwise, N_j being the total number of particles. Making use of (2.1) within a Monte Carlo framework, we evaluate the probability that the contaminant concentration at a given well is lower than a given threshold, C^*, varying λ_i and t. As an example, Figure 2.2 reports the results obtained on the basis of 100 Monte Carlo realizations for $t \to \infty$, i.e. the maximum (long-term) expected concentration, versus λ_i varying the land use. The results reveal very low contaminant recovery at North-East Bologna area, Figure 2.2(j-l). This result is related to the long residence times (low velocities) occurring in this area of the site (see Deliverable 2.3 for details). On the other hand, we note that the San Vitale well field is characterized by non-negligible concentrations of contaminants released from the agricultural land (see Figure 2.2) even when the degradation rate is high.

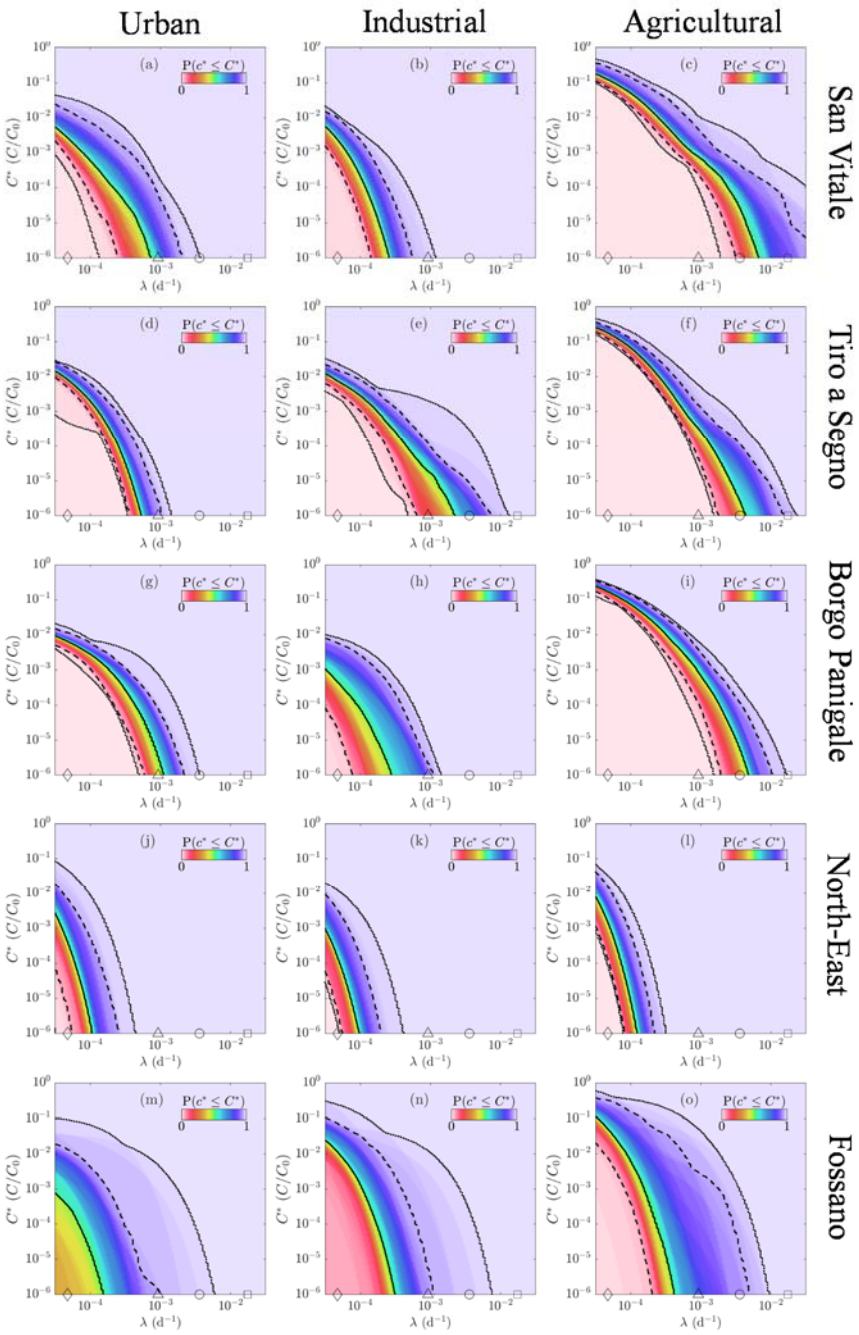

Figure 2.2. Probability that $C_{i,j}(t \to \infty) < C^*$ versus the reaction rate λ. Left to right, the different plots correspond to diverse contaminant sources (Urban, Industrial, and Agricultural). From top to bottom, the plots correspond to different wells or well groups (San Vitale, Tiro a Segno, Borgo Panigale, wells located in the North-East area of Bologna, and Fossano). The degradation rates for four selected contaminants (see Section 2.2) are highlighted: PFOS (diamond), Carbendazim (triangle), triclosan (circle) and acetaminophen (square). Black curves indicate: 50% (solid curve), 5 - 95% (dashed curves), 1%- 99% (dotted curves) percentiles.

2.2 Risk assessment approach including complex interactions

The results obtained in Section 2.1, and in particular $C_i = C_i(t \to \infty)$, can then be used to estimate the human health risk associated with polluted groundwater consumption, in different scenarios.

Two types of human health risk metrics are usually considered. The first is used for compounds inducing non-carcinogenic systemic effects, either through short- or long-term exposures. It is sometimes known as Hazard Quotient in human health risk and it is defined, for a compound i as:

$$R_{\text{tox},i} = \frac{C_i}{C_{\text{ref},i}}, \tag{2.2}$$

where C_i is the concentration of compound i (M L^{-3}), and $C_{\text{ref},i}$ is a reference concentration value above which consumption of compound i could have negative effects on humans. The second type is the carcinogenic risk and should be used when there are evidences that compounds may induce carcinogenic effects to humans

$$R_{\text{can},i} = \kappa \gamma_i C_i, \tag{2.3}$$

where κ is the expected long-term consumption rate of water per body weight unit ($\text{L}^3\ \text{M}^{-1}\ \text{T}^{-1}$), and γ_i is the cancer potency factor (T), typically expressed as a reciprocal dose (e.g., $(\text{mg Kg}^{-1}\text{d}^{-1})^{-1}$).

The typical limits for each individual compound i are $R_{\text{tox},i} < 1$ and $R_{\text{can},i} < 10^{-h}$, with 5 or 6 being the most typical choices for h. Note that in both cases the human health risk posed by compound i is proportional to the concentration C_i, (directly or indirectly) compared to a reference concentration. Hereafter, we denote the risk simply as R_i, representing either of these two definitions.

In the event that N compounds with an associated risk to human health are found in the same water, there are two basic approaches to determine the risk associated with the mixture in the absence of complex interactions. The first of these models is called Independent Action (IA) and it is based on the assumption that the modes of action of each compounds are different and independent. In this case, the mixture risk R_* is calculated as:

$$R_* = 1 - \prod_{i=1}^{N} (1 - R_i)\,. \tag{2.4}$$

Another possible (more conservative) assumption is that the different sources of risk to human health follow similar modes of action and hence add up arithmetically. This model is known as Concentration Addition (CA) and R_* is evaluated as

$$R_* = \sum_{i=1}^{N} R_i \,. \tag{2.5}$$

Note that, in the case of carcinogenic risk, since risks are typically much smaller than 1, these two models are nearly equivalent.

Several studies (e.g., Jonker et al., 2005) have shown that, oftentimes, the actual combined risk does not behave as predicted by equation (2.4) or (2.5). In some cases, the combined risk is found to be significantly higher than predicted by CA or IA. This indicates synergy between chemicals. In other cases, the combined risk can be lower than predicted by CA or IA, indicating antagonism between chemicals.

A simple yet popular model to represent synergy and antagonism effects for $N = 2$ reads

$$R = R_* \exp(-a z_1 z_2)\,, \tag{2.6}$$

where

$$z_i = \frac{R_i}{R_1 + R_2}. \tag{2.7}$$

The parameter a represents the strength and the sign of the chemical interaction: a negative value represents synergism, whereas a positive value represents antagonism. In case $a = 0$, then $R = R_*$ and we recover the original CA or IA behavior. Embedding (2.6) within a Monte Carlo framework, it is then possible to estimate the probability that the risk is smaller than a given threshold (R) varying a. An example of the results is offered by Figure 2.3, where this probability has been evaluated for the Bologna site considering two interacting contaminants, one injected over the industrial and urban areas and one over the agricultural areas. Both contaminants are characterized by $C_0 = 0.01$ mg/L, $C_{\text{ref}} = C_0$, $\lambda = 10^{-3}$, and the hazard quotient with interaction is computed by expressions (2.2) and (2.5). Moving along the horizontal axis corresponds to modifying the chemical interaction towards a purely additive ($a = 0$), synergistic ($a < 0$) or antagonistic ($a > 0$) behavior.

The results show that the risk of groundwater contamination is, in some cases, highly sensitive to the complex toxic non-additivity of compounds coming from different land use types. This is particularly true in Tiro a Segno (Figure 2.3(b)) and Fossano (Figure 2.3(e)). The latter shows a very high variability in the results, with a low percentile going beyond the $R = 1$ limit for $a \ll 0$. Other locations (see Figure 2.3(a,c)) are less sensitive to the chemical interaction in this case. Finally, the risk is negligible in North-East area of Bologna (Figure 2.3(d)) due to its high degree of isolation from the aquifer top (see Deliverable 2.3).

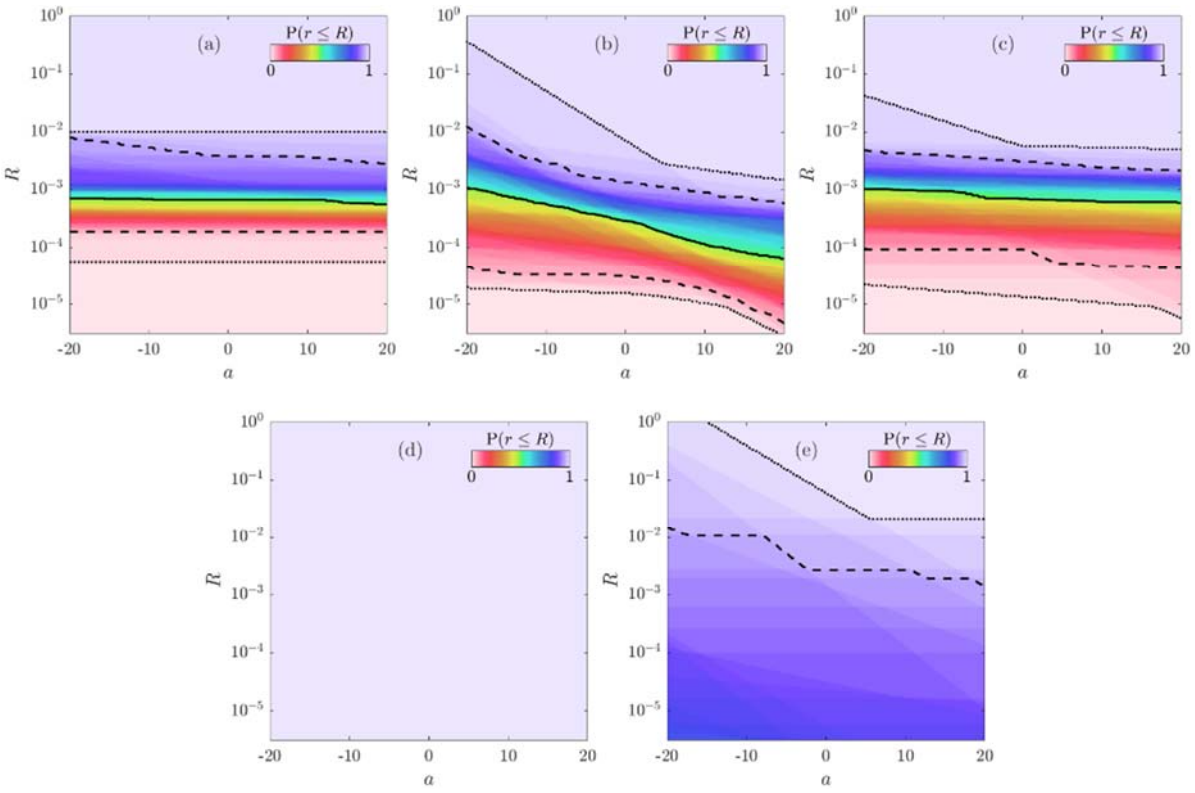

Figure 2.3: Probability that the combined risk is smaller than R versus a, for two contaminants of different source (Urban/Industrial, Agricultural). The different plots correspond to different wells or well groups: (a) San Vitale, (b) Tiro a Segno, (c) Borgo Panigale, (d) North-East area of Bologna, and (e) Fossano.

The risk calculation can be applied to specific contaminants using values from the literature. We choose four representative emerging contaminants: Acetaminophen, Triclosan, PFOS, and Carbendazim. A summary of their relevant properties is given in Table 2.1. The values of NOAEL are given as a proxy for their toxicity. Usually, one would estimate the reference concentration for human consumption by extrapolation from non-human data. In this case, the reference concentration is divided by a safety factor (e.g., 1000) that depends on the type of extrapolation and the typical weight and water consumption of a person. Here, we write the input concentrations as some multiple of C_{ref}, hence the results shown below do not depend on the choice of the safety factor.

More complex interaction models than (2.6) have been proposed (Jonker et al., 2005), which allow to consider dose-ratio or dose-level dependent deviations from additivity. The toxicity studies performed in the context of this project, as well as the literature review, showed only antagonistic effects (either pure antagonistic, or more complex descriptions such as dose-level or dose-ratio dependent antagonisms) between the chosen emerging contaminants. Therefore, in the following implementation of the probabilistic risk assessment with actual substances, we simply use additivity (CA, equation (2.5)), in order to follow a conservative approach.

Table 2.1: Emerging contaminants considered in the risk assessment

	Acetaminophen	Triclosan	PFOS	Carbendazim
Source type	Urban	Urban	Industrial	Agricultural
λ ($\cdot 10^{-5}$ d^{-1})	347 [1*]	34.7 [2]	4.75 [3]	92.4 [4]
NOAEL (mg/kg·d, anim)	500 [5]	25 [6]	0.03 [7]	5 [8]

[1]Hillebrand et al., 2015, [*]Reduced by a safety factor of 100 because experiments were in strictly aerobic conditions, [2]Tixier et al., 2002, [3]US EPA, 2014, [4]Yu et al., 2009, [5]Venkatesan et al., 2014, [6]Borzelleca et al., 1992, [7]Seacat et al., 2002, [8]Stadler,1986.

We analyze the sensitivity of the results by varying both model inputs (C_0 and λ). All the considered input concentrations are well below the compounds' solubility. The results are depicted in Figure 2.4 for three percentiles of the Monte Carlo collection of results: 50% (p50), 95% (p95) and 99% (p99). It can be clearly observed that PFOS (PFS) is the main contributor to the risk, which can be explained by its very low degradation rate (see table 2.1). The well that is the most sensitive to this kind of contamination is Fossano (Fno), because of the high contribution of industrial land to its capture zone (see Deliverable 2.3). Carbendazim (CBZ) also contributes significantly to the risk. In some cases (for example, TaS in Figure 2.4(k)), additivity of PFS and CBZ can produce values of $R > 1$, while each contaminant individually does not infringe its respective reference value. Small contributions to the total risk are also observed for Triclosan (TCS). No significant contribution is observed from Acetaminophen (AMP), which has the highest degradation rate among the four contaminants considered.

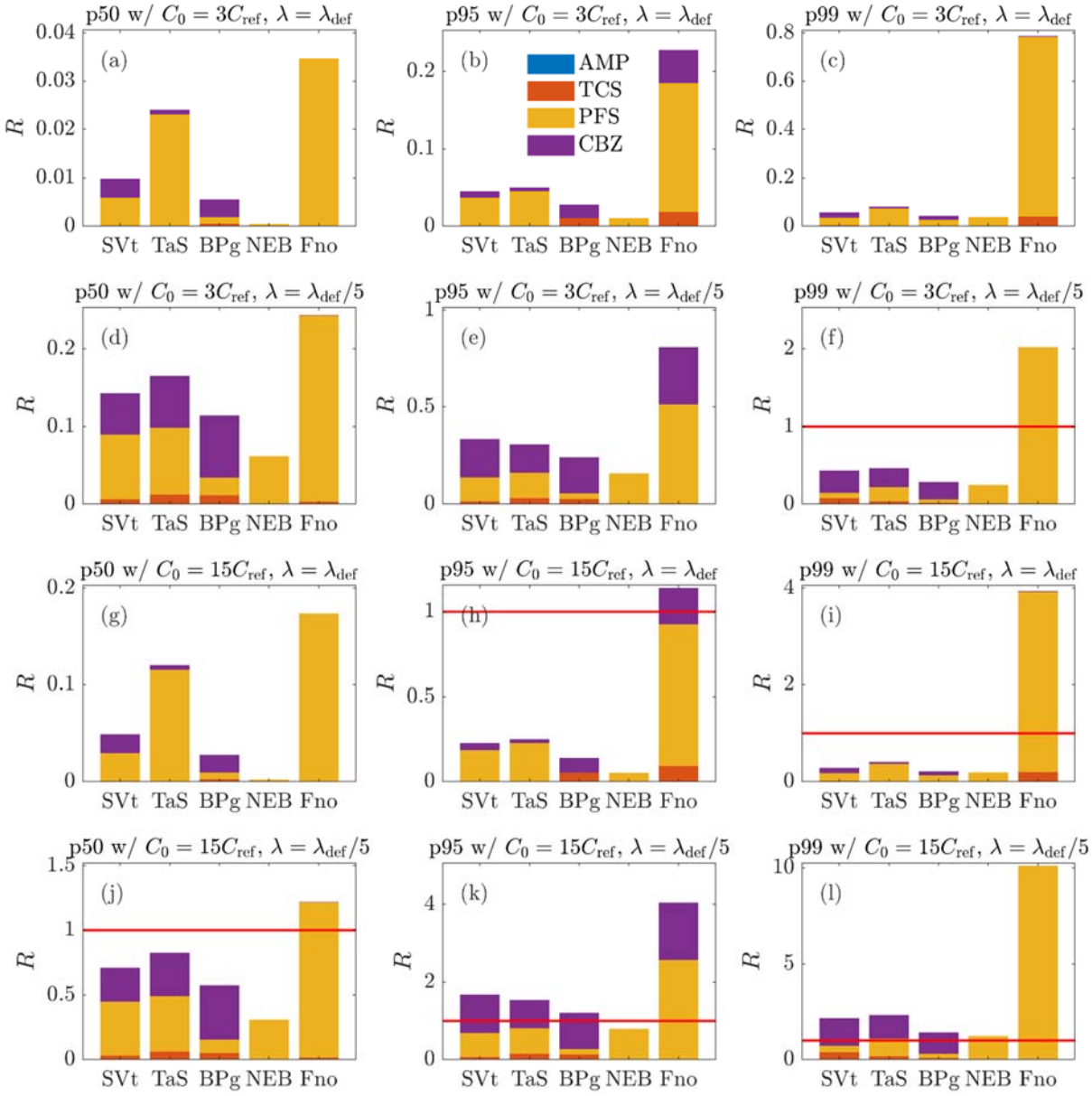

Figure 2.4: Risk (equations (2.5)) evaluated at the different wells or well groups (horizontal axis, SVt = San Vitale, TaS = Tiro a Segno, BPg =Borgo Panigale, NEB =North-East area of Bologna, and Fno = Fossano) for various percentiles from left to right, and various configurations of C_0 and λ from top to bottom ("w/"≡"with"). The colors in the bars indicate the contribution of each contaminant to the total risk. The horizontal red line indicates the $R = 1$ limit.

3. Cremona site

A key feature of the Cremona aquifer is the occurrence of natural high-quality water springs which are the main supply to agriculture and a key environmental driver. These natural springs (and the associated historical buildings and hydraulic works) have remarkable social, historical and touristic value. Springs contribute to a set of interconnected, natural and delicate ecosystems, hosting plants and animal life fully adapted to their water quality. This system constitutes an example of a delicate environment in need of preservation. Over recent years, excessive extraction has caused progressive lowering of the groundwater table, producing a documented decrease in spring flow rates, causing spring depletion in some case. For this reason, the application of the GPRM to Cremona field site has be devoted to identify new sustainable groundwater management strategies for the protection and preservation of the natural springs' environment. The problem is exemplified in Figure 3.1.

The final goal of the envisioned management model is finding the maximum value of well pumping rate, Q, not leading to spring depletion. GPRM allows to account for multiple sources of uncertainty in our knowledge and description of the system.

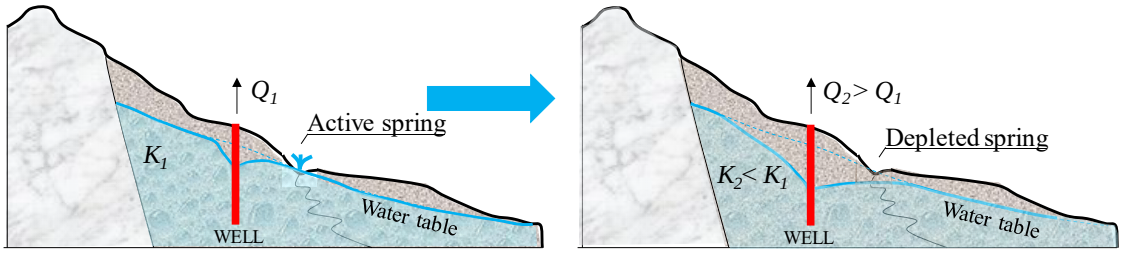

Figure 3.1. Scheme of spring depletion.

3.1 Groundwater management model under uncertainty

In order to develop and apply a GPRM (see Deliverable 5.1) to the Cremona site we need to define the following key objects: (1) 'Model predictions', (2) 'System Failure event', (3) 'Design variables' and (4) 'Source of Uncertainty'. Here:

(1) Model predictions are the system responses in terms of hydraulic head, h, values at the spring location. Values of h are obtained using the three-dimensional groundwater flow models developed within WP1 and WP2 (Deliverables 1.4a-b, 2.2 and 2.3). In particular, two probabilistic models are considered: *Composite Medium* (*CM*) and *Overlapping Continua* (*OC_A*) model. *CM* considers each block of the numerical grid as formed by a geomaterial. *OC_A* is grounded on the concept that the system can be viewed as formed by a collection of media coexisting in space (see Deliverables D1.4a-b).

(2) System Failure event, *SF*, is identified with the depletion of at least one spring within the domain. Note that *SF* depends on economical/social constraints and must be set with the support of the stakeholders/decision makers on the basis of the most relevant-crucial points in the system. In this case, due to the area under investigation that is crucial not

only for economical purposes but also for touristic activities, we implement the GPRM in order to preserve all active springs.

(3) Design variables are associated with the flow rate of a set of selected pumping wells within the domain.

(4) We consider two sources of uncertainty (a) Conceptual Model and (b) Model parameters' uncertainty. Conceptual Model Uncertainty is included in our GPRM by considering diverse reconstructions of the Cremona geological features (see also point 1). Model parameters' uncertainty are N_p log-conductivity values, Y_i=logk_i, associated with most influential geomaterials constituting the aquifer system (see Deliverable 1.4b). i.e. Y_i values associated with (*i*) clay, gravel and fractured conglomerate for *CM*, rendering N_p = 3 and (*ii*) gravel and fractured conglomerate for *OC_A*, rendering N_p = 2.

The formulation of the groundwater management strategy is associated with a constrained optimization problem. The primary objective of this optimization is maximizing the total groundwater volume extracted from the aquifer per unit time subject to the constraints on the hydraulic head monitored at springs' location. These issues are summarized in Eqs. (3.1)-(3.3)

$$\text{maximize} \quad \sum_{i=1}^{N_w} Q_i \tag{3.1}$$

$$Q_i^{\min} \le Q_i \le Q_i^{\max} \tag{3.2}$$

$$h_j\left(\mathbf{Q},\mathbf{Y}\right) - h_{TR,j} > 0 \qquad j = 1,...,N_s \tag{3.3}$$

Here, $\mathbf{Q}$ is a vector containing the flow rate of each pumping well, Q_i, (with i = 1,…, N_w); $\mathbf{Y}$ is a vector of Y_i values (i =1, N_p); N_w is the number of pumping wells; $h_j\left(\mathbf{Q},\mathbf{Y}\right)$ is the hydraulic head at spring j predicted by the numerical model using the log-conductivity field associated with $\mathbf{Y}$ and the pumping flow rate $\mathbf{Q}$; $h_{TR,j}$ is the threshold (minimum hydraulic head) associated with the j-th spring ; N_s is the number of springs. The flow rate vector $\mathbf{Q}$ is allowed to vary within the interval $\left[\mathbf{Q}^{\min},\mathbf{Q}^{\max}\right]$ where $\mathbf{Q}^{\min}$ and $\mathbf{Q}^{\max}$ indicate vectors respectively containing lower ($Q_i^{\min}$) and upper ($Q_i^{\max}$) bounds of Q_i. The outflow-rate of the j-th spring, $Q_{s,j}$, is evaluated as

$$Q_{s,j} = \begin{cases} A\dfrac{K_d}{e}\left(h_j - h_{0,j}\right) & h_j > h_{0,j} \\ 0 & h_j \le h_{0,j} \end{cases} \tag{3.4}$$

where $h_{0,j}$ is the springs bottom elevation, A is the planar area of the spring, K_d and e being the hydraulic conductivity and the thickness of the drain bed, respectively (see also Deliverable 1.4b). Quantities K_d and e allow to evaluate leakage coefficient $l_d = K_d/e$ which has been assumed constant in space and has been calibrated for *CM* and *OC_A* models in Deliverable

1.4b and 2.3. The threshold $h_{TR,j}$ is evaluated from (3.4) to ensure a minimum flow rate $Q_{s,j}^{\min}$, as

$$h_{TR,j} = h_{0,j} + Q_{s,j}^{\min} / (A\, l_d) \tag{3.5}$$

$Q_{s,j}^{\min}$ must be set on the basis of economic and social constrains. Here, for illustration purpose we assumes $Q_{s,j}^{\min}$ constant for each spring, i.e. $Q_s^{\min}$.

The vector **Y** has been calibrated through a Maximum Likelihood (ML) approach (see Deliverable 1.4b and 2.3), rendering a mean value ($\boldsymbol{\mu}$) of **Y** as well as a posterior covariance matrix ($\boldsymbol{\Sigma}$). We therefore consider **Y** as an N_p-uncertain parameters' vector, characterized by a multivariate gaussian distribution with mean ($\boldsymbol{\mu}$) and covariance ($\boldsymbol{\Sigma}$).

The constrained optimization problem (Eqs 3.1-3.3) is solved using a standard trust region method based on interior point techniques (Byrd et al., 2000). This procedure requires, for a selected log-conductivity field, about 300 runs of the forward model demanding about 20 hours on a personal computer with a 3.20 GHz Core(TM) i7-6900K CPU in our test cases. Therefore, considering the complete groundwater model to simulate the hydraulic head at the spring locations significantly limits the number of multiple realizations of the optimization problems which are computationally feasible. For this reason, we evaluate the system response, in terms of hydraulic head at the spring location, relying on a surrogate model based on the generalized Polynomial Chaos Expansion (gPCE) (Ghanem and Spanos, 1991; Xiu and Karniadakis, 2002; Le Maître and Knio, 2010). This technique (see also Deliverable 1.4b) allows approximating $h_j(\mathbf{Q},\mathbf{Y})$ by a linear combination of multivariate orthonormal Legendre polynomials, i.e., $\psi_{\boldsymbol{x}}(\boldsymbol{p})$, with $\boldsymbol{p} = [\mathbf{Q},\mathbf{Y}]$, having dimension $M = N_p + N_w$, as

$$\begin{aligned} f(\boldsymbol{p}) &\cong f_0 + \sum_{i=1}^{M} \sum_{\boldsymbol{x}\in\Im_i} \beta_{\boldsymbol{x}} \psi_{\boldsymbol{x}}(\boldsymbol{p}) + \sum_{i=1}^{M}\sum_{j=1}^{M} \sum_{\boldsymbol{x}\in\Im_{i,j}} \beta_{\boldsymbol{x}} \psi_{\boldsymbol{x}}(\boldsymbol{p}) + \ldots; \\ \psi_{\boldsymbol{x}}(\boldsymbol{p}) &= \prod_{i=1}^{M} \psi_{i,x_i}(p_i); \quad \beta_{\boldsymbol{x}} = \int_{\Gamma} f(\boldsymbol{p}) \psi_{\boldsymbol{x}}(\boldsymbol{p}) \rho_{\Gamma_{\boldsymbol{p}}}\, d\boldsymbol{p}, \end{aligned} \tag{3.6}$$

where $\boldsymbol{x} = \{x_1, \ldots, x_M\} \in \mathrm{N}^M$ is a multi-index expressing the degree of each univariate polynomial, $\psi_{i,x_i}(p_i)$; $\beta_{\boldsymbol{x}}$ are the gPCE coefficients; $\rho_{\Gamma_{\boldsymbol{p}}}$ is the pdf of **p**; $\Im_i$ contains all indices such that only the *i*-th component does not vanish; $\Im_{i,j}$ contains all indices such that only the *i*-th and *j*-th components are not zero, and so on, $\boldsymbol{\Gamma} = [\mathbf{p}^{\min}, \mathbf{p}^{\max}]$ indicates the parameter space where $\mathbf{p}^{\min}$ and $\mathbf{p}^{\max}$ are vectors respectively containing lower ($p_i^{\min}$) and upper ($p_i^{\max}$) bounds of parameter variability intervals. Coefficients $\beta_{\boldsymbol{x}}$ in Eq. (3.6) are evaluated through a regression-based method (Sudret, 2008). The latter requires to compute the full model and its gPCE approximation at a number of points in the parameter space, and then minimizing the sum of the square of the differences between the exact and the approximated solutions. Here,

accurate results have been obtained truncating the gPCE at order 3 (see Annex I), requiring N_t = 1115 simulations for *CM* model and N_t = 720 simulations for *OC_A* approach (due to the different number of input parameters) performed using a quasi-Monte Carlo sampling technique (see e.g., Feil et al., 2009; Fajraoui et al., 2012; Maina and Guadagnini, 2018). The ability of a gPCE to approximate hydraulic heads at the target points (i.e., locations corresponding to the springs) is assessed considering a set of N_t/10 points not employed for the evaluation of the gPCE. Results of this analysis (shown in Annex I) shows that the gPCE provides good approximation of the full model results being satisfactory for the purpose of our analysis.

For the application of GPRM to the Cremona site, we implement the methodology described below and shown in the flow chart of Figure 3.2:

(1) We sample the $\mathbf{Y}$ distribution $N = 10^4$ times, obtaining N Monte Carlo realizations of the log conductivity field.

(2) We solve the optimization problem Eqs (3.1)-(3.3) N times

(3) As a result of step (2) we obtain a sample of size N of best flow rates, $\hat{\mathbf{Q}}_n = \left[\hat{Q}_{n,1},\cdots,\hat{Q}_{n,Nw}\right]$, with n = 1,…N. Each $\hat{\mathbf{Q}}_n\left(\mathbf{Y}_n\right)$ corresponds to a particular realization of the conductivity field (resulting from $\mathbf{Y}_n$) and indicates the maximum flow rates which are allowed to withdrawn from each well in order to avoid the depletion of any spring in the n-th Monte Carlo realization.

(4) $\hat{\mathbf{Q}}_n\left(\mathbf{Y}_n\right)$ obtained at step (3) allow to subdivide the log-conductivity Monte Carlo realizations in the following three regions:

(i) Region A. It includes realizations $\mathbf{Y}_n$ for which the constrain (3.3) is never satisfied. In other words, the depletion of at least one spring is observed even when the minimum pumping rate is set at all pumping wells (System Failure, *SF*, always detected).

(ii) Region B. It includes realizations $\mathbf{Y}_n$ associated with $Q_i^{\min} < \hat{Q}_{n,i} < Q_i^{\max}$ at least in one well.

(iii) Region C. It includes realizations $\mathbf{Y}_n$ for which $\hat{Q}_{n,i} = Q_i^{\max}$ in all pumping wells (*SF* never detected).

(5) On the bases of step (4) we evaluate the probability of *SF*, as detailed in section 3.2

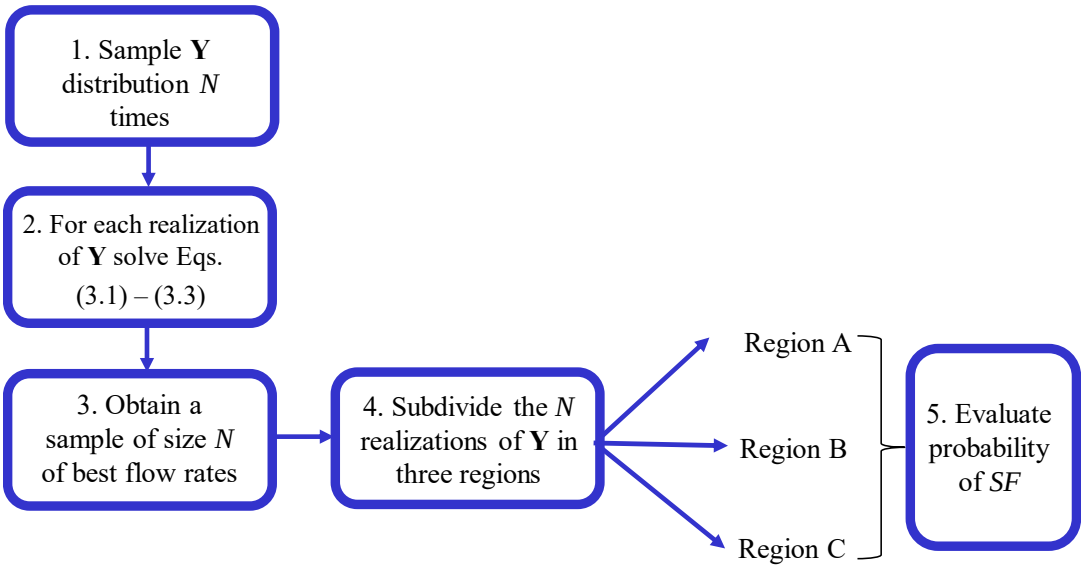

Figure 3.2. Flow chart of the methodology for the application of GPRM to the Cremona site.

3.2 Fault tree analysis

Here, we focus on Fault tree analyses (FTA) (Bedford and Cooke, 2003; Tartakowsky 2007; Fernàndez-Garcia et al. 2012) to evaluate the probability of *SF*. A generic fault tree consists of different potential events, whose inter-connections can be represented with Boolean operators. Once a fault tree is constructed, the probability of each individual event must be evaluated. This in turn enables the evaluation of the overall probability of *SF*. We apply the general methodology discussed in Deliverable 5.1 to our case study, where *SF* occurs when for at least in one spring (amongst those considered in the analysis) the hydraulic head drops below the threshold, i.e., $h_j(\mathbf{Q},\mathbf{Y}) - h_{TR,j} < 0$ (see Eq. 3.3). The basic relevant events for our analysis and their notation are listed in Table 3.1.

Event	**Notation**
Log-conductivities belonging to Region A	*YA*
Log-conductivities belonging to Region B	*YB*
The hydraulic head simulated for at least one spring is smaller than the threshold.	$h_{TR,j} > h_j$

Table. 3.1. Glossary of event abbreviation

The chain of events which lead to *SF* is graphically represented in Figure 3.3. The Boolean representations of this fault tree is

$$SF = YA + YB \cdot \left(h_{TR,j} > h_j\right) \tag{3.7}$$

Equation (3.7) allows to identify the failure modes of our system, also called *minimal cut sets of the system*, i.e., the smallest collections of events leading to at least the depletion of one spring. The fault tree in Figure 3.3 and Eq. 3.7 reveals two minimal cuts (M_1 and M_2):

- M_1: {The log-conductivity **Y** belongs to region A}
- M_2: {The log-conductivity **Y** belongs to region B. For at least one spring the hydraulic head predicted by the model is lower than the threshold}.

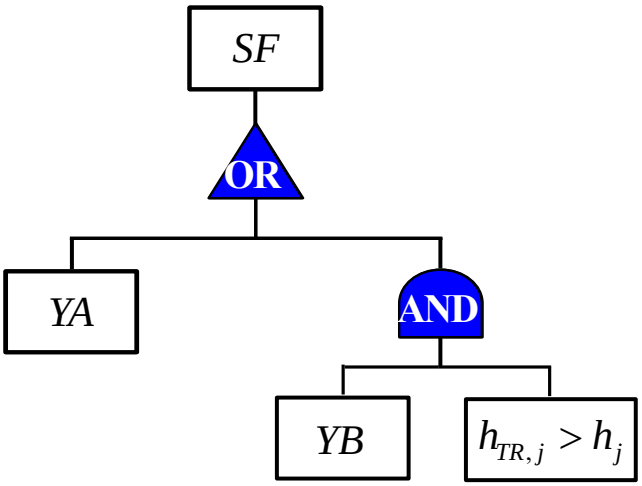

Figure 3.3. Fault tree of the spring failure problem

The probability of *SF*, *P*[*SF*], is then given by the inclusion exclusion law of probability as

$$P[SF] = P[M_1] + P[M_2] - P[M_1 \cdot M_2] \tag{3.8}$$

Since there is no intersection between Region A and Region B the minimal cut sets M_1 and M_2 do not overlap each other and we obtain:

$$P[M_1] = N_A / N \tag{3.9}$$

$$P[M_2] = N_B / N \cdot P\left[h_{TR,j} > h_j\right] \tag{3.10}$$

$$P[M_1 \cdot M_2] = 0$$

Where N_A and N_B indicate, respectively, the number of sample points in Region A and Region B. Substituting Eqs. (3.9) - (3.11) in Eq. (3.8) we obtain:

$$P\left[SF\right] = \frac{N_A}{N} + \frac{N_B}{N} \cdot P\left[h_{TR,j} > h_j\right] \tag{3.12}$$

3.3 Data set

We apply the methodology proposed in Sections 3.1 and 3.2 by selecting $N_w = 5$ pumping wells located in the zone of highest spring density within the Cremona area. We then apply the hydraulic head constraint to the $N_s = 34$ natural springs closer to these wells. Location of pumping wells and springs is reported in Figure 3.4 and Annex II. We introduce the following additional variables: (*i*) the sum of all 5 optimal flow rates normalized by the associated

maximum value: $Q^T = \frac{1}{N_w}\sum_{i=1}^{N_w} Q_i / Q_i^{\max}$; (*ii*) the sum of normalized flow rates of two wells in the Northern sector, i.e., Arzago (BG) and Misano (BG), $Q^N = \frac{1}{2}\sum_{i=1}^{2}\left(Q_i / Q_i^{\max}\right)$ and the sum of normalized optimal flow rates in the remaining three wells in the Southern area, i.e. Capralba (CR), Sergnano (CR) and Spino (CR), $Q^S = \frac{1}{3}\sum_{i=3}^{5}\left(Q_i / Q_i^{\max}\right)$.

Considering Q^T , a lower bound of $P[SF]$ corresponds to

$$P[SF] = \frac{N_A}{N} + \frac{N_B}{N} F_{\hat{Q}^T}\left(Q^T\right) \tag{3.12}$$

where $F_{\hat{Q}^T}\left(Q^T\right)$ is the empirical cumulative density function, *cdf*, of $\hat{Q}^T$ (evaluated within the Region B).

Considering Q^N and Q^S upper and lower bound of $P[SF]$ can be evaluated respectively as:

$$P[SF] = \frac{N_A}{N} + \frac{N_B}{N}\left[F_{\hat{Q}^N}\left(Q^N\right) + F_{\hat{Q}^S}\left(Q^S\right) - F_{\hat{Q}^N,\hat{Q}^S}\left(Q^N, Q^S\right)\right] \tag{3.13a}$$

$$P[SF] = \frac{N_A}{N} + \frac{N_B}{N} P\left[\hat{Q}^N + \hat{Q}^S < Q^N + Q^S\right] \tag{3.13b}$$

where $F_{\hat{Q}^N}\left(Q^N\right)$, $F_{\hat{Q}^S}\left(Q^S\right)$ and $F_{\hat{Q}^N,\hat{Q}^S}\left(Q^N, Q^S\right)$ are respectively the marginal empirical *cdf* of the variables $\hat{Q}^N$ and $\hat{Q}^S$ and the joint empirical *cdf* of the variables $\hat{Q}^N$ and $\hat{Q}^S$ (evaluated within the Region B).

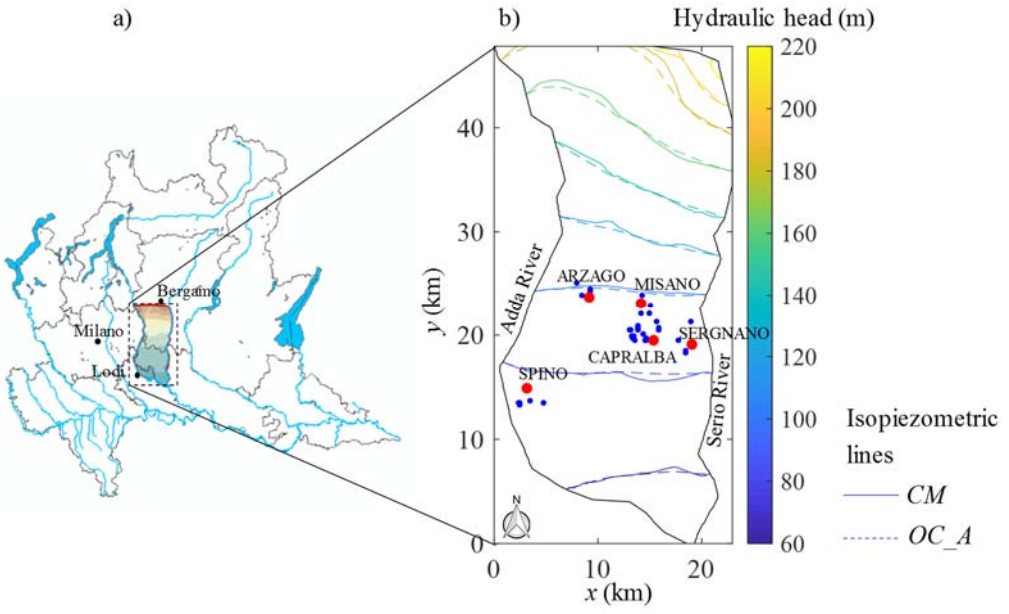

Figure 3.4. a) Location of wells and springs considered in the analysis; b) hydraulic head distributions of the calibrated models, continuous and dotted lines are associated respectively with *CM* and *OC_A*.

3.4 Results and discussion

According to the results of the GSA, in Deliverable 1.4a, we calibrate parameters k_1, k_3 and k_5 for *CM* and k_3, k_5 for *OC_A* using a ML approach. For each conceptual model, insensitive parameters are fixed to values consistent with the geological features of the corresponding classes, as reported in Table 2.5 of Deliverable 1.4a. As calibration data, we considered yearly-averaged hydraulic head values collected at 35 observation wells during year 2015 (location of these wells is reported in Figure 2.1a of Deliverable 2.3). ML estimates ($\boldsymbol{\mu}$) of the log-transformed calibrated parameter ($Y_i=\log k_i$) and estimation error covariance matrices ($\boldsymbol{\Sigma}$) are reported in Table 3.2.

Groundwater Model	ML estimates	Estimation error covariance matrix
CM	$\boldsymbol{\mu}=\left[-4.39,-1.67,-1.92\right]$	$\boldsymbol{\Sigma}=\begin{bmatrix} 1.62\times10^{-3} & -2.57\times10^{-3} & 4.90\times10^{-3} \\ \cdots & 3.63\times10^{-2} & -1.40\times10^{-2} \\ \cdots & \cdots & 2.65\times10^{-2} \end{bmatrix}$
OC_A	$\boldsymbol{\mu}=\left[-1.74,-2.00\right]$	$\boldsymbol{\Sigma}=\begin{bmatrix} 2.60\times10^{-2} & 2.07\times10^{-2} \\ \cdots & 6.07\times10^{-2} \end{bmatrix}$

Table 3.2. Statistical parameters of the multivariate normal distributions considered in the analysis.

Figure 3.5 compares the prior (Uniform) probability density function, *pdf*, of each parameter against the (marginal) posterior (Gaussian) counterpart. ML estimates are consistent with the geological features of the classes (see Deliverable D1.4b and D2.3). Lowest values are associated with clay (Class 1), while the largest conductivities are related to gravel and fractured conglomerate (Classes 3 and 5).

Contour lines of bivariate *pdfs* are depicted in Figure 3.6 a-c for *CM* and in Figure 3.6d for *OC_A*. Figure 3.6, as well as Table 3.2, indicates slightly negative correlation between the parameter pairs Y_1-Y_3 (Figure 3.6a), negative correlation between Y_3-Y_5 (Figure 3.6b) and slightly positive correlation between the pair Y_1-Y_5 (Figure 3.6c) for *CM* approach. Considering *OC_A*, Y_3 and Y_5 are positively correlated (Figure 3.6d).

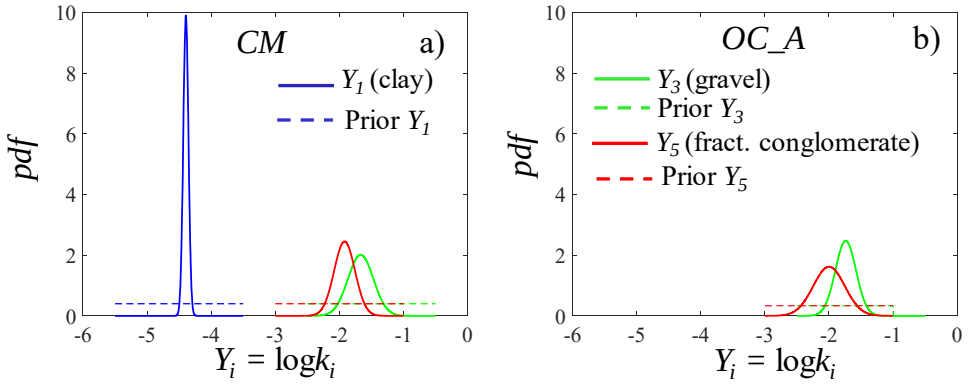

Figure 3.5. Prior and marginal posterior *pdf* of calibrated parameters for a) *CM* and b) *OC_A* approach.

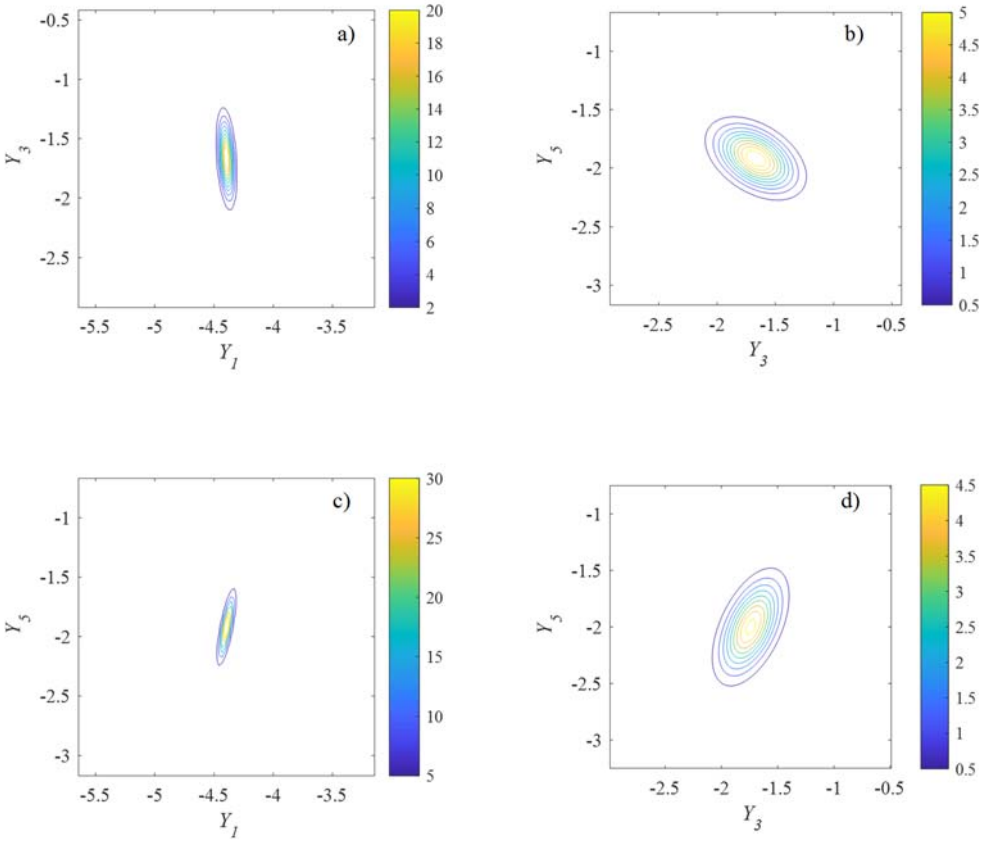

Figure 3.6 Contour lines of bivariate *pdfs* of calibrated parameters considering *CM* (a) Y_1 - Y_3; (b) Y_3 - Y_5; (c) Y_1 - Y_5 and *OC_A* (d) Y_3 - Y_5.

The samples of $N = 10^4$ data points, randomly extracted from the multivariate normal distributions of Table 3.2, are depicted in Figure 3.7.

Then, following the procedure described in Section 3.1, we compute a sample of size N of best flow rates $\hat{\mathbf{Q}}_n = \left[\hat{Q}_{n,1},\cdots,\hat{Q}_{n,Nw}\right]$ (with n = 1,…N) as well as $\hat{Q}_n^T = \frac{1}{5}\sum_{i=1}^{N_w=5}\hat{Q}_{n,i}/Q_i^{\max}$, $\hat{Q}_n^N = \frac{1}{2}\sum_{i=1}^{2}\hat{Q}_{n,i}/Q_i^{\max}$ and $\hat{Q}_n^S = \frac{1}{3}\sum_{i=3}^{5}\hat{Q}_{n,i}/Q_i^{\max}$ by allowing, in each well, the flow rate to vary between 0 and 1 m^3/sec and by ensuring a minimum flow rate at each spring, $Q_s^{\min}$, equal to 0.13 m^3/s, corresponding to 75% of the value of the calibrated model.

Relying on $N = 10^4$ allows us to obtain stable statistic measures of the quantity of interest, i.e. of $\hat{\mathbf{Q}}$, $\hat{Q}^T$, $\hat{Q}^N$ and $\hat{Q}^S$, as shown in Annex III.

In our test cases we attain: N_A = 4105 and N_B = 3443 for *CM*; and N_A =3143 and N_B = 3453 for *OC_A*. The number of points in Region C can be evaluated as $N_C = N - N_A - N_B$ and is equal to 2452 for *CM* and 3404 for *OC_A*. Regions A, B and C in the considered parameter spaces are depicted in Figure 3.8 with blue, red and green points, respectively. We note N_A is larger for *CM* than for *OC_A*, i.e. Region A of the parameter space, where the constraints cannot be satisfied, is larger for *CM* than for *OC_A*. This result is consistent with the observation that (considering the results reported in Deliverable 1.4b and 3.2) the calibrated leakage coefficient l_d (see Eq. 3.5) is larger for *OC_A* than for *CM*, being respectively equal to 1.21 × 10^{-6} s^{-1} and 1.30 × 10^{-6} s^{-1}. Therefore, setting the same $Q_s^{\min}$ (see Eq. 3.5) for the two models, leads to (on average) values of $h_{TR,j}$ smaller for *OC_A* than for *CM*. Incidentally, we further note that Region A could be neglected in the evaluation of $P[SF]$ (Eqs. 3.12-3.13), whenever water is detected.

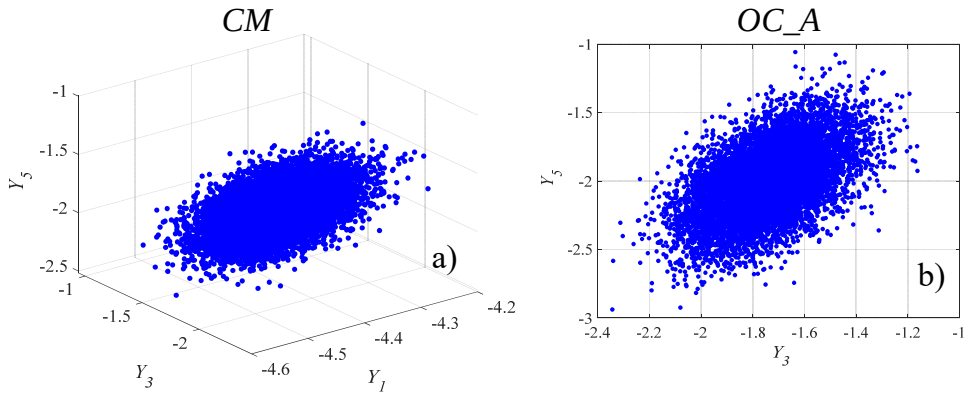

Figure 3.7. Sample of size $N = 10^4$ from the multivariate *pdfs* of the parameter estimates for a) *CM* and b) *OC_A* approaches.

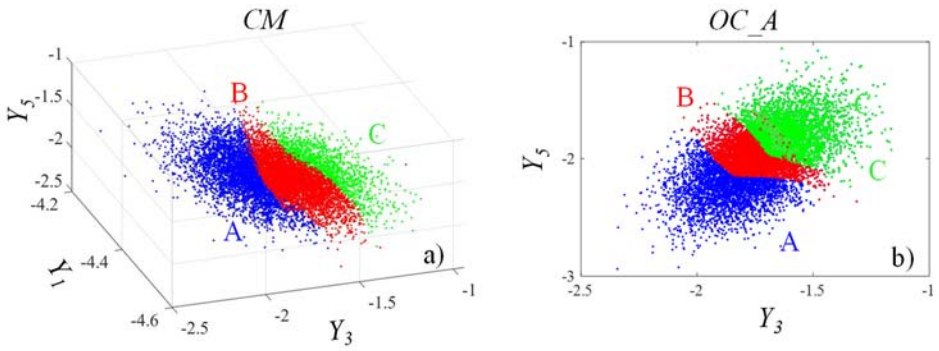

Figure 3.8. Map of Region A (blue dots), Region B (red dots) and Region C (green dots) obtained on the sample of Figure 3.7 for a) *CM* and b) *OC_A* approach.

Figure 3.9 depicts empirical *cdfs* of the variables $\hat{Q}_i / Q_i^{\max}$ with $i = 1,\ldots, N_w$ and of the variable $\hat{Q}^T$ within Region B considering *CM* (3.9a) and *OC_A* (3.9b). Note that the *cdfs* associated with a single well flow rate are in general different depending on the selected well and on the adopted modeling approach while the *cdf* of $\hat{Q}^T$ tends to be similar for the two conceptual models. The relative frequency of the variables $\hat{Q}_i / Q_i^{\max}$ ($i = 1,\ldots, N_w$) and of $\hat{Q}^T$ evaluated within Region B is shown in Figures 3.10a-b for *CM* and *OC_A* respectively. These distributions show that uncertainty in **Y** values has strong impact on the evaluation of the optimal flow rates. Contour lines of empirical bivariate *cdfs*, $F_{\hat{Q}_i,\hat{Q}_j}\left(Q_i, Q_j\right)$, with $i = 1,...,N_w - 1$, $j = 2,...,N_w$ and $j > i$, are depicted in Figures 3.11 and 3.12 for *CM* and *OC_A* respectively. Note than the conceptual model strongly affects the shape of these *cdf*s.

The lower bound of the Probability of system failure, $P[SF]$, is evaluated as a function of Q^T via Eq. (3.12) and depicted in Figure 3.13 for the two conceptual models (continuous curves). The two curves present a similar slope, however lower bound of $P[SF]$ is larger for *CM* than for *OC_A*, for each value of Q^T. This is related to the fact that, as we mentioned above, N_A in *CM* is larger than its counterpart evaluated for *OC_A*. The dotted curves in Figure 3.13 represent the case when all the springs in the domain are active and $P[SF]$ is evaluated as $P[SF] = N_B / (N - N_A) \cdot F_{\hat{Q}^T}\left(Q^T\right)$. In this case, the probability of *SF* obtained with the two analyzed geological models is very similar, i.e. the uncertainty in the conceptual model adopted can be neglected for the evaluation of the lower bound of $P[SF]$.

Considering *CM* model, lower and upper bounds of $P[SF]$ are evaluated as a function of Q^N and Q^S via Eqs. 3.13b-c and depicted in Figures 3.14a-b. Note that the lower bound of $P[SF]$ gives the same failure probability to each pairs $Q^N + Q^S = \text{constant}$ (Figure 3.14a) while its upper bound (Figure 3.14b) includes information obtained from the solution of the optimization problem described in Section 3.1. The difference between upper and lower bounds is depicted in Figure 3.14c and presents its maximum value close to the corners of the domain.

Both lower and upper bounds of $P[SF]$ are always smaller than 1 since $N_C > 0$ and larger than zero since $N_A > 0$. Figures 3.14d-e represent the cases when all the springs in the domain are active and lower and upper bounds of $P[SF]$ are evaluated, respectively, as

$$P[SF] = \frac{N_B}{N - N_A} P\left[\hat{Q}^N + \hat{Q}^S < Q^N + Q^S\right]$$

$$P[SF] = \frac{N_B}{N - N_A}\left[F_{\hat{Q}^N}\left(Q^N\right) + F_{\hat{Q}^S}\left(Q^S\right) - F_{\hat{Q}^N,\hat{Q}^S}\left(Q^N, Q^S\right)\right].$$

Analogous results for *OC_A* are depicted in Figure 3.15 not showing particular differences from its *CM* counterparts.

Figure 3.16 reports the upper bound conditional probabilities $P[SF|\,Q^N = 0.25, 0.5, 0.75]$ (dotted lines) and $P[SF|\,Q^S = 0.25, 0.5, 0.75]$ (continuous lines). These results shows that for both modeling approach upper bound of $P[SF]$ is slightly more influenced by Q^N (continuous curves), while variability in Q^S (dotted curves) impact $P[SF]$ only to a lesser extent in particular for $Q^N > 0.5$. These findings indicate that, to further improve the management of the groundwater pumping at the site, one should primary focus on the pumping wells in the northern sector of the analyzed system.

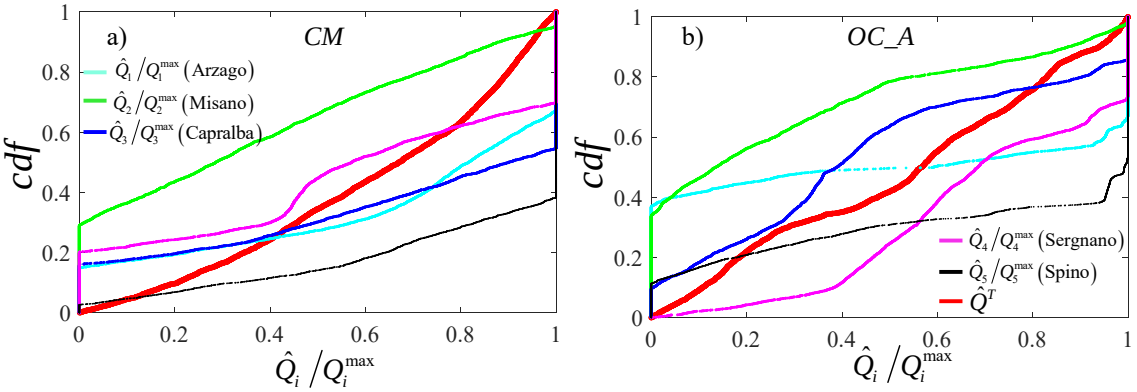

Figure 3.9. Marginal *cdf* of the variables $\hat{Q}_i/Q_i^{\max}$ ($i = 1,\ldots,N_W$) and $\hat{Q}^T$ evaluated within Region B.

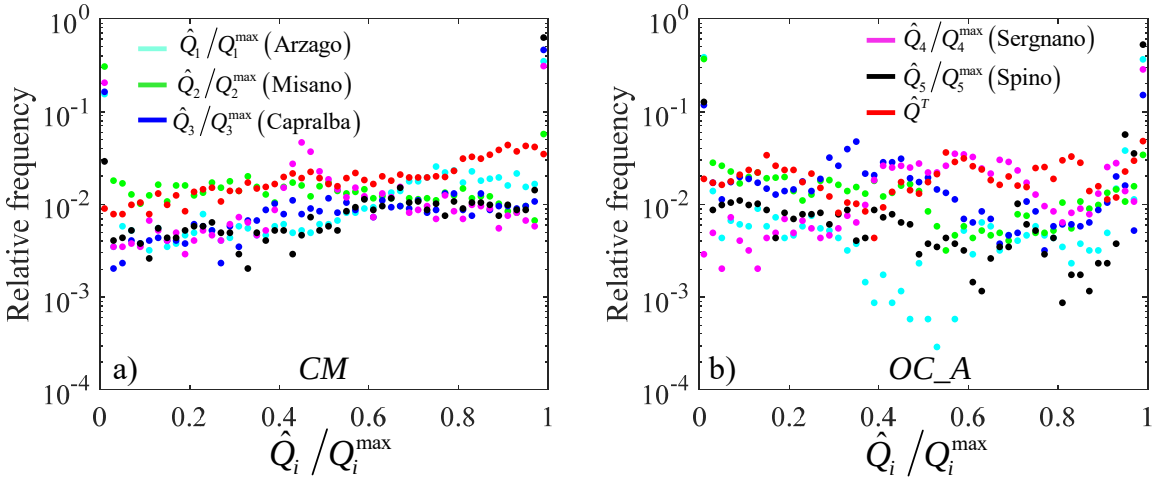

Figure 3.10. Relative frequency of the variables $\hat{Q}_i/Q_i^{max}$ ($i = 1,\ldots,N_w$) and $\hat{Q}^T$ evaluated within Region B.

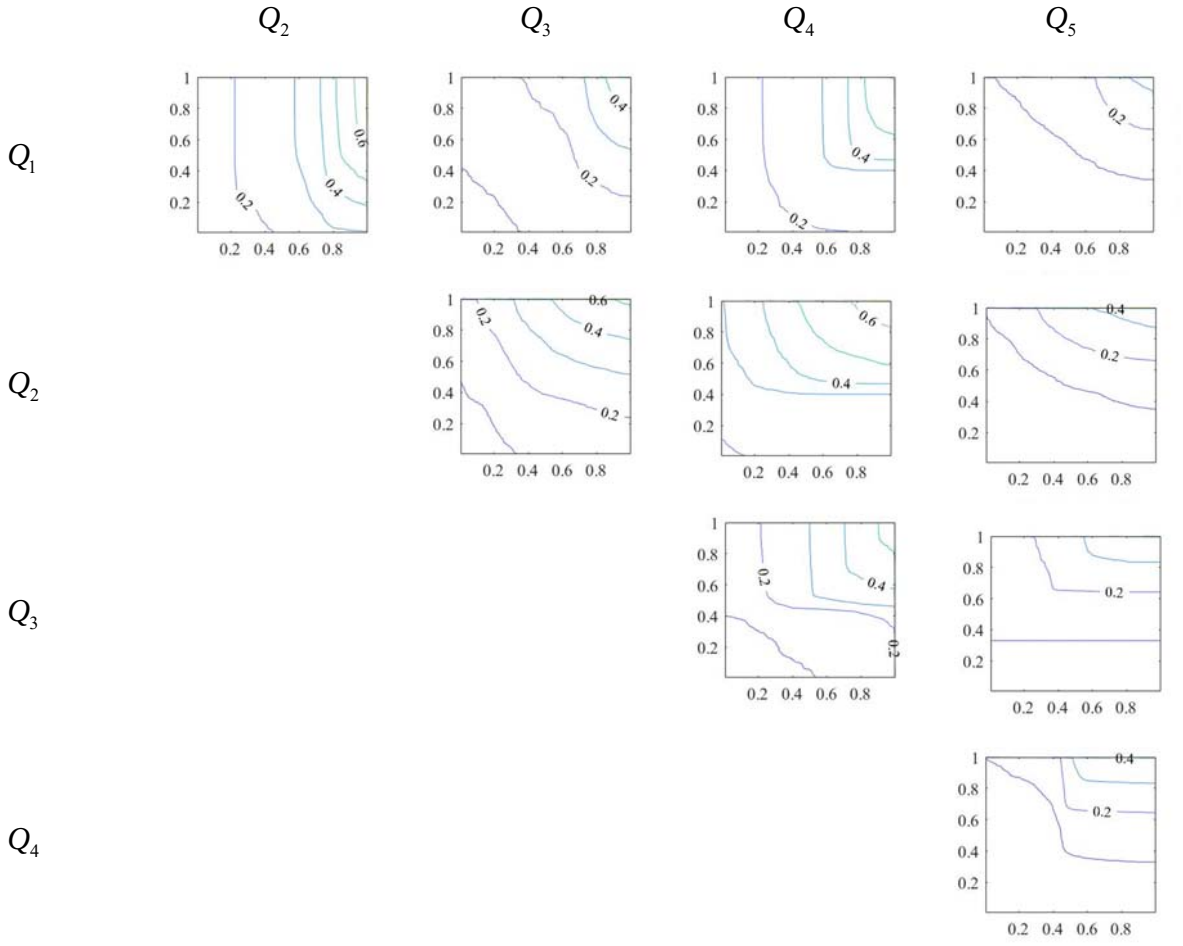

Figure 3.11. Empirical joint cumulative distribution functions, $F_{\hat{Q}_i,\hat{Q}_j}(Q_i,Q_j)$, with i =1-4, j =2-5 and $j > i$, for *CM*.

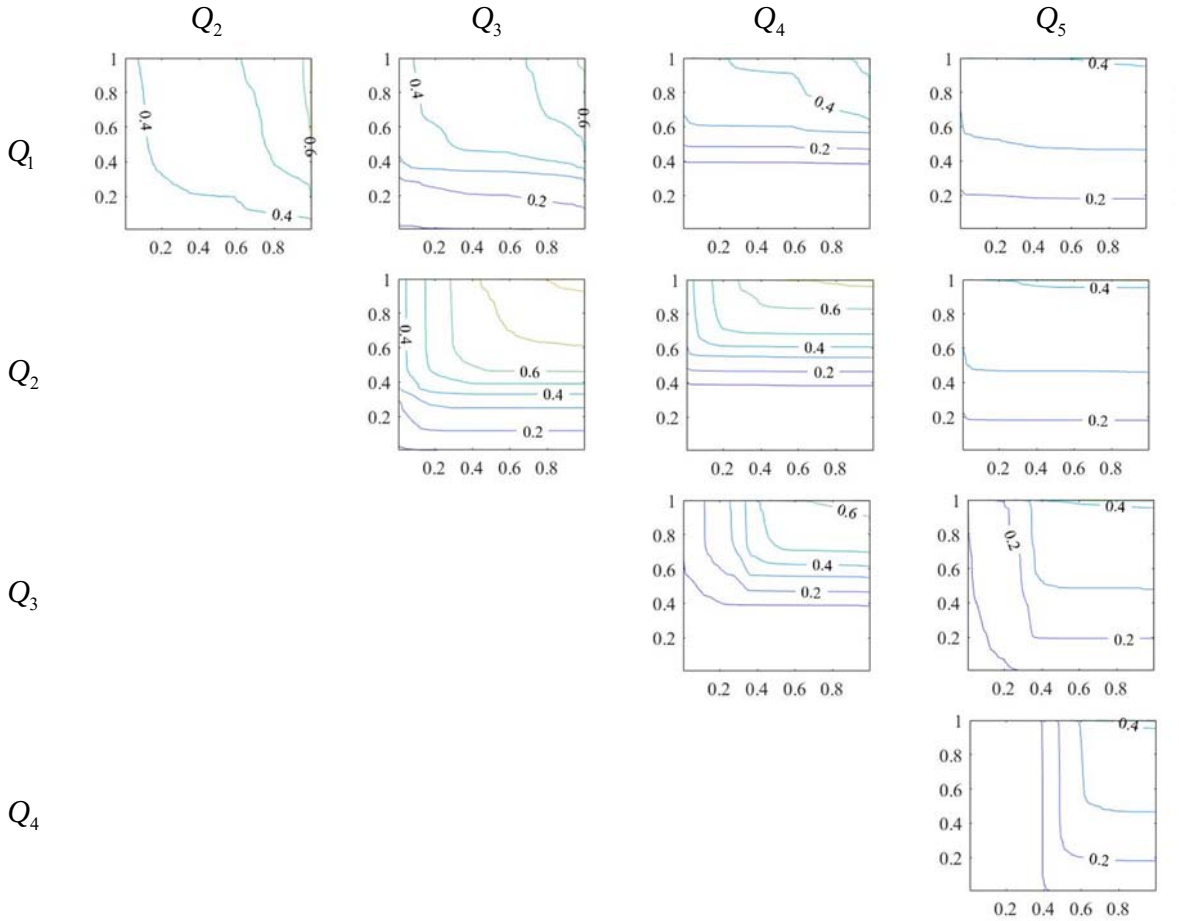

Figure 3.12. Empirical joint cumulative distribution functions, $F_{\hat{Q}_i,\hat{Q}_j}\left(Q_i,Q_j\right)$, with i =1-4, j =2,5 and $j > i$, for *OC_A*.

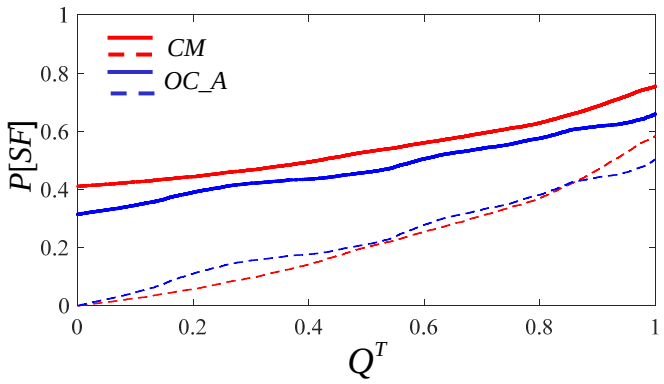

Figure 3.13. Lower bound of probability of *SF* as a function of Q^T (Eq. 3.12). Red and blue curves depict results related to *CM* and *OC_A* models, respectively. Dotted curves indicate *P*[*SF*] when all the springs in the domain are active.

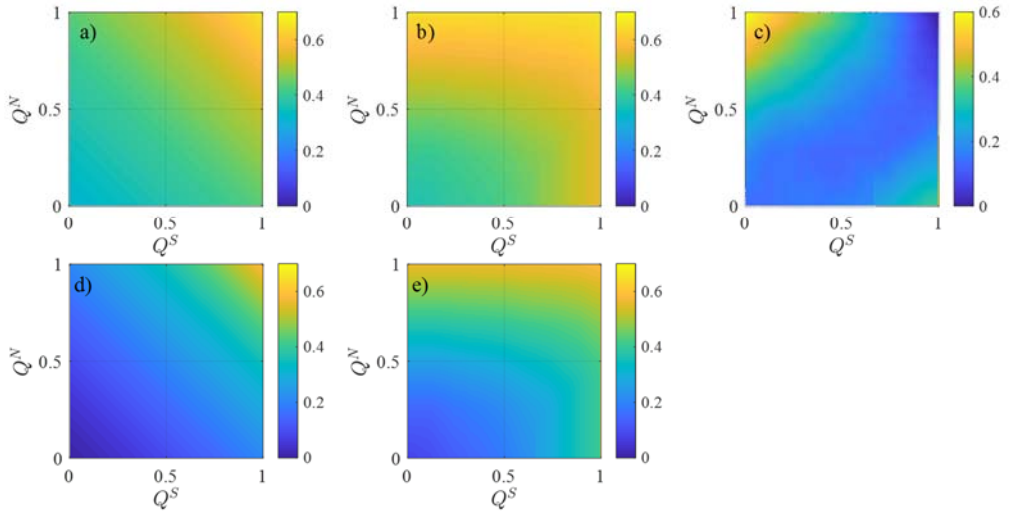

Figure 3.14. *CM*: a) lower bound of $P[SF]$ as a function of Q^S and Q^N (Eq. 3.13a); b) upper bound of $P[SF]$ as a function of Q^S and Q^N (Eq. 3.13b); c) difference between upper and lower bound of $P[SF]$ d) lower bound of $P[SF]$ when all the springs in the domain are active and e) upper bound of $P[SF]$ when all the springs in the domain are active.

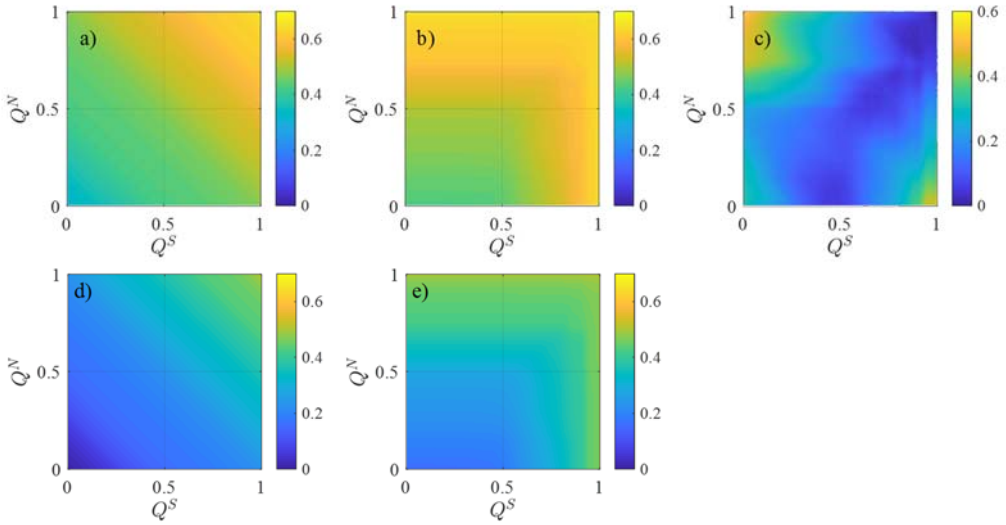

Figure 3.15. *OC_A* a) lower bound of $P[SF]$ as a function of Q^S and Q^N (Eq. 3.13a); b) upper bound of $P[SF]$ as a function of Q^S and Q^N (Eq. 3.13b); c) difference between upper and lower bound of $P[SF]$ d) lower bound of $P[SF]$ when all the springs in the domain are active and e) upper bound of $P[SF]$ when all the springs in the domain are active.

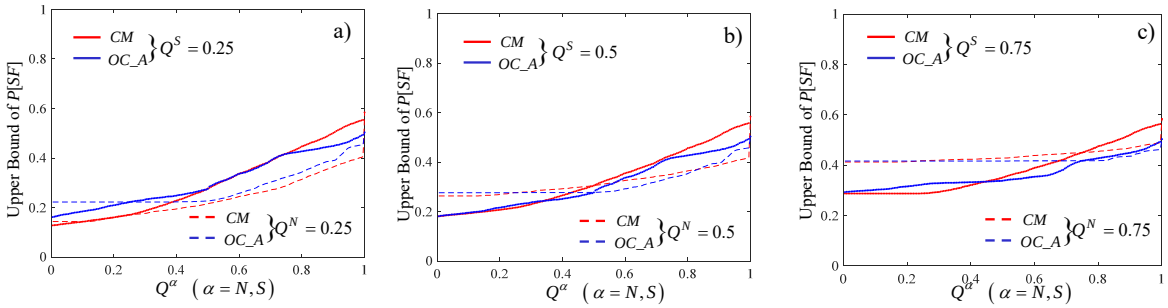

Figure 3.16. Cross section of upper bound of *P*[*SF*] shown in Figure 3.14b and 3.15b a) at $Q^S = 0.25$ (continuous lines) and $Q^N = 0.25$ (dotted lines); b) at $Q^S = 0.5$ (continuous lines) and $Q^N = 0.5$ (dotted lines); c) at $Q^S = 0.75$ (continuous lines) and $Q^N = 0.75$ (dotted lines). Red and blue lines are associated with *CM* and *OC_A*, respectively

The relative frequency, *F,* of hydraulic head values at the 34 spring locations is shown in Figure 3.17 and 3.18 for *CM* and *OC_A* respectively. Statistical metrics (i.e., mean, variance and coefficient of variation, CV) of these hydraulic head values are reported in Table 3.3 and 3.4 for *CM* and *OC_A*, respectively. The name of each spring is associated with the closest well amongst the 5 considered (exact location of each spring is reported in Table A.2, Annex II). Red and green bars depict distribution within Region B and C, respectively. Note that head distributions within region B are characterized by a peak close to the head threshold while their counterpart within region C are characterized by higher spread (variance) and lower peaks (at values larger than the thresholds). Overall Figures 3.12 and 3.13, show that: (*i*) hydraulic head variability at springs due to uncertainty in log-conductivities is (on average) larger for *OC_A* than for *CM* approach (see also Table 3.3); (*ii*) hydraulic head variability is higher in the Norther with respect to the Southern sector for both models; (*ii*) at some springs the hydraulic head never reaches the imposed threshold. Therefore, Figure 3.12 and 3.13 also allows to identify the most vulnerable springs, where depletion first occurs.

	Mean (m)		Variance (m^2)		CV	
	Region B	**Region C**	**Region B**	**Region C**	**Region B**	**Region C**
Ar-1	97.82	97.93	0.005	0.006	0.001	0.001
Ar-2	98.57	98.66	0.006	0.006	0.001	0.001
Ar-3	99.05	99.14	0.005	0.005	0.001	0.001
Ar-4	100.60	100.66	0.003	0.003	0.001	0.001
Mi-1	92.88	93.07	0.007	0.024	0.001	0.002
Mi-2	92.85	93.02	0.004	0.017	0.001	0.001
Mi-3	95.05	95.19	0.004	0.013	0.001	0.001
Mi-4	98.12	98.23	0.008	0.013	0.001	0.001
Ca-1	87.86	88.20	0.027	0.061	0.002	0.003
Ca-2	87.64	87.94	0.020	0.053	0.002	0.003
Ca-3	87.62	87.91	0.019	0.053	0.002	0.003
Ca-4	88.26	88.60	0.027	0.060	0.002	0.003
Ca-5	87.99	88.28	0.018	0.050	0.002	0.003
Ca-6	88.64	88.98	0.027	0.058	0.002	0.003
Ca-7	88.61	88.95	0.026	0.058	0.002	0.003
Ca-8	88.60	88.94	0.025	0.057	0.002	0.003
Ca-9	88.82	89.11	0.017	0.046	0.001	0.002
Ca-10	89.81	90.13	0.021	0.048	0.002	0.002
Ca-11	89.79	90.11	0.021	0.048	0.002	0.002
Ca-12	89.68	89.98	0.017	0.043	0.001	0.002
Ca-13	89.63	89.82	0.007	0.023	0.001	0.002
Ca-14	90.06	90.34	0.016	0.040	0.001	0.002
Ca-15	90.01	90.20	0.006	0.021	0.001	0.002
Ca-16	90.44	90.71	0.014	0.036	0.001	0.002
Ca-17	91.17	91.34	0.005	0.016	0.001	0.001
Se-1	84.80	84.99	0.011	0.026	0.001	0.002
Se-2	85.26	85.44	0.010	0.025	0.001	0.002
Se-3	87.73	87.89	0.006	0.017	0.001	0.001
Se-4	91.47	91.52	0.000	0.001	0.000	0.000
Sp-1	72.79	72.88	0.002	0.004	0.001	0.001
Sp-2	73.03	73.13	0.003	0.004	0.001	0.001
Sp-3	73.05	73.16	0.003	0.005	0.001	0.001
Sp-4	73.61	73.80	0.010	0.015	0.001	0.002
Sp-5	73.59	73.74	0.006	0.011	0.001	0.001

Table 3.3. Mean, variance and CV of hydraulic heads at the spring locations within Region B and C for *CM*.

	Mean (m)		Variance (m^2)		CV	
	Region B	**Region C**	**Region B**	**Region C**	**Region B**	**Region C**
Ar-1	97.93	98.20	0.031	0.069	0.002	0.003
Ar-2	98.89	99.19	0.050	0.103	0.002	0.003
Ar-3	99.45	99.75	0.055	0.109	0.002	0.003
Ar-4	101.11	101.36	0.042	0.078	0.002	0.003
Mi-1	93.17	93.56	0.037	0.150	0.002	0.004
Mi-2	93.31	93.70	0.038	0.140	0.002	0.004
Mi-3	95.68	96.06	0.071	0.178	0.003	0.004
Mi-4	98.76	99.13	0.117	0.236	0.003	0.005
Ca-1	86.63	87.14	0.030	0.147	0.002	0.004
Ca-2	86.67	87.12	0.023	0.134	0.002	0.004
Ca-3	86.67	87.11	0.022	0.134	0.002	0.004
Ca-4	87.08	87.61	0.032	0.148	0.002	0.004
Ca-5	87.15	87.60	0.022	0.134	0.002	0.004
Ca-6	87.55	88.08	0.031	0.148	0.002	0.004
Ca-7	87.54	88.06	0.031	0.149	0.002	0.004
Ca-8	87.54	88.06	0.030	0.147	0.002	0.004
Ca-9	88.10	88.56	0.022	0.135	0.002	0.004
Ca-10	89.03	89.54	0.028	0.142	0.002	0.004
Ca-11	89.02	89.53	0.027	0.143	0.002	0.004
Ca-12	88.99	89.48	0.024	0.142	0.002	0.004
Ca-13	89.28	89.67	0.015	0.098	0.001	0.004
Ca-14	89.47	89.95	0.024	0.141	0.002	0.004
Ca-15	89.77	90.16	0.016	0.099	0.001	0.004
Ca-16	89.99	90.46	0.023	0.139	0.002	0.004
Ca-17	91.27	91.68	0.021	0.108	0.002	0.004
Se-1	84.15	84.42	0.006	0.030	0.001	0.002
Se-2	84.62	84.88	0.006	0.031	0.001	0.002
Se-3	87.10	87.39	0.007	0.041	0.001	0.002
Se-4	91.41	91.59	0.003	0.012	0.001	0.001
Sp-1	72.83	72.99	0.005	0.007	0.001	0.001
Sp-2	73.10	73.26	0.005	0.007	0.001	0.001
Sp-3	73.12	73.29	0.005	0.008	0.001	0.001
Sp-4	73.54	73.81	0.014	0.027	0.002	0.002
Sp-5	73.69	73.91	0.010	0.017	0.001	0.002

Table 3.4. Mean, variance and CV of hydraulic heads at the spring locations within Region B and C for *OC_A*.

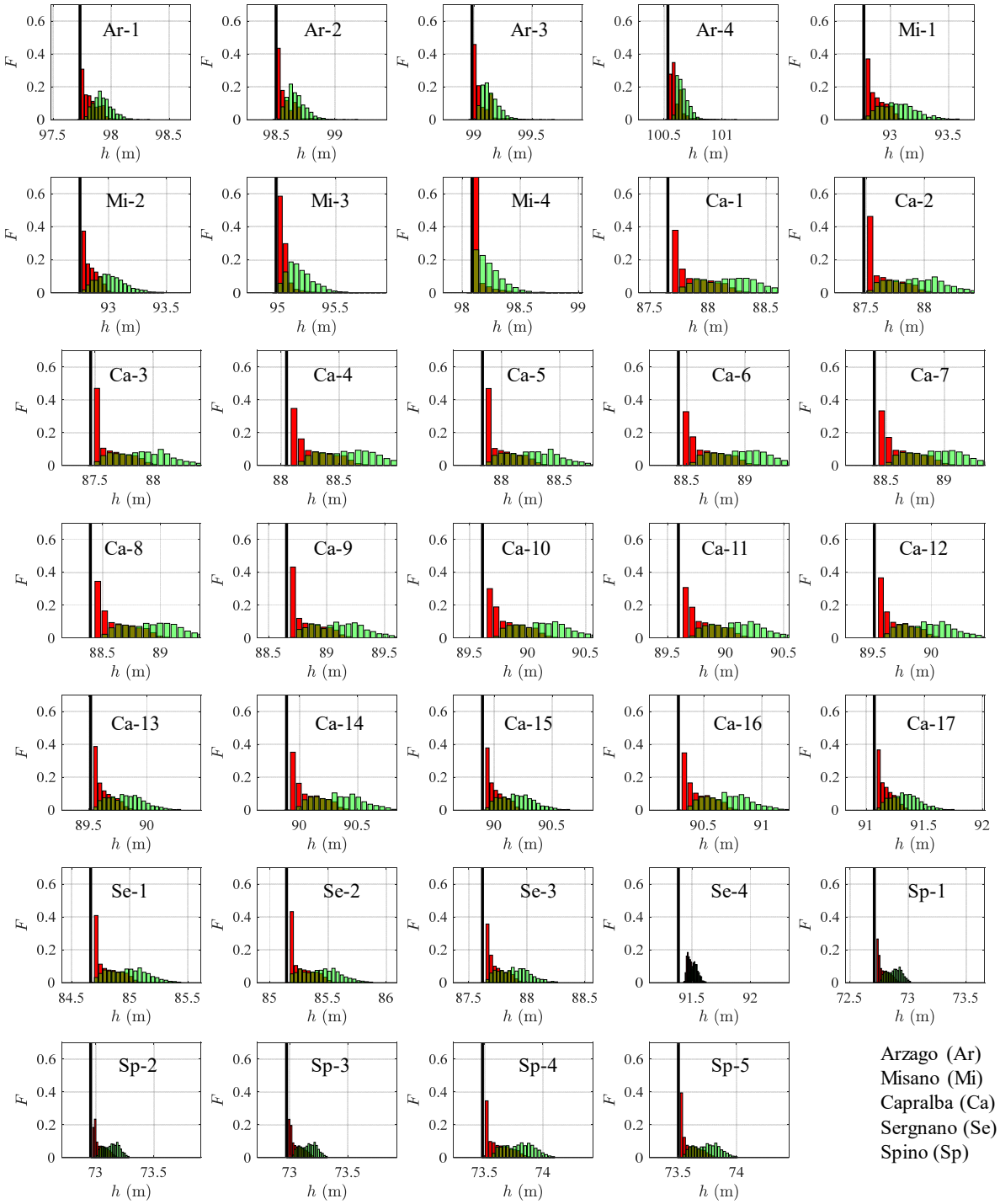

Figure 3.17. Hydraulic heads distribution at spring's locations for *CM*. Red and green bars depict distribution within Region B and C, respectively. The black vertical line indicates the hydraulic head threshold at each spring.

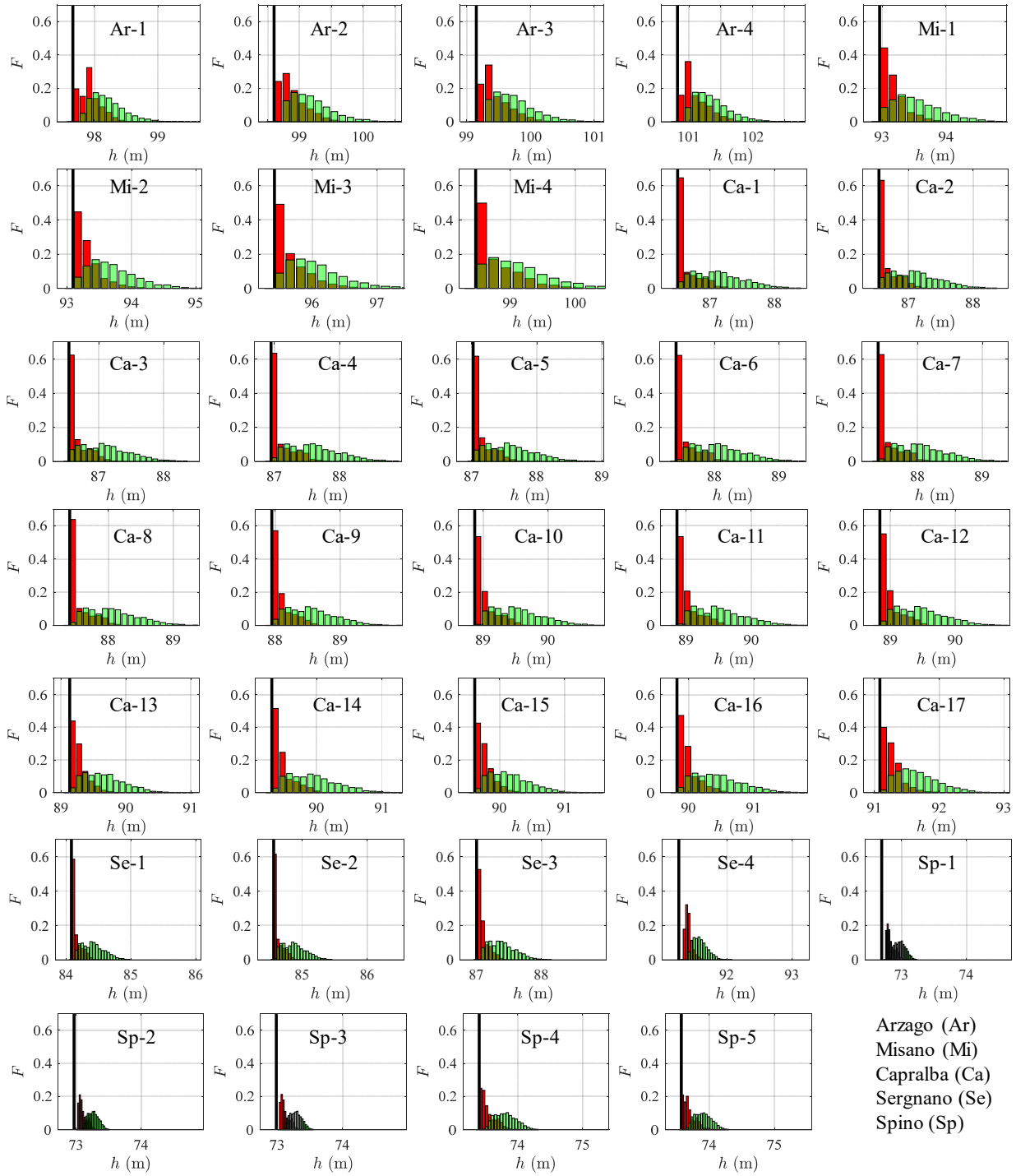

Figure 3.18. Hydraulic heads distribution at spring's locations for OC_A. Red and green bars depict distribution within Region B and C, respectively. The black vertical line indicates the hydraulic head threshold at each spring.

4. Conclusions and final remarks

Our results show that the application the GPRM to the pilot sites can be successful for assessing (and preventing) negative issues related to water resources management and exploitation.

Considering the Bologna site, we combine different sources of information (geological, hydrological, geographical) to build a stochastic model from which one can infer the likelihood of contaminants' concentration to exceed threshold values. That allows us to estimate the risk of contamination associated with simultaneous contaminating activities within a probabilistic framework. Our analysis allows to conclude that (i) different wells in the basin extract groundwater with a different land-use signature, i.e. they are vulnerable to different types of contamination; (ii) hypothetical non-additive synergies between contaminants of different land-use signature would affect the risk posed to human health, especially at Tiro a Segno and Fossano well sites; (iii) no significant risk has been found for four tested emerging contaminants to reach any of the wells at dangerous concentrations; and (iv) PFOS and Carbendazim (in this order) have the highest associated risks, and Fossano is the most vulnerable well site.

For the Cremona site, we combine a wide range of data to promote improved governance of groundwater by balancing economic issue (maximizing well extraction rates) and environmental sustainability (avoiding spring depletion). The application of GPRM to the Cremona site allows (i) to quantify the risk associated with spring depletion due to increasing exploitation of the aquifer; (ii) to quantify how different sources of uncertainty (conceptual model uncertainty and model parameters' uncertainty) affects this risk; (iii) to determine the optimal wells' flow rates; and (iv) to identify the most vulnerable springs, where depletion first occurs.

References

Bedford T., Cooke R., 2003. Probabilistic Risk Analysis: Foundations and Methods. Cambridge Univ. Press. New York.

Byrd R.H., Gilbert J.C., Nocedal J., 2000. A trust region method based on interior point techniques for nonlinear programming. Mathematical Programming. 89. (1). 149-185.

Borzelleca J.F., Frankos V.H., Johnson E.M., Jordan W., Squire R.A., Weill C., 1992. Report of the expert panel on the safety of tricosan on toothpaste and oral rinse products. Environ Corporation Expert Panel Report.

de Barros F.P.J., Bolster D., Sanchez-Vila X., Nowak W., 2011. A divide and conquer approach to cope with uncertainty. human health risk. and decision making in contaminant hydrology. Water Resour. Res. 47 (5). W05508.

Deliverable 1.4a, 2018. Report on characterization of field sites, WE-NEED.

Deliverable 1.4b, 2018. Report on characterization of field sites, WE-NEED.

Deliverable 2.2, 2018. Report on groundwater flow and transport on the two field sites, WE-NEED.

Deliverable 2.3, 2019. Report on probabilistic time related protection zones of the two field sites, WE-NEED.

Deliverable 5.1, 2018. Report on groundwater risk management model, WE-NEED.

Fajraoui N., Mara T.A., Younes A., Bouhlila R., 2012. Reactive transport parameter estimation and global sensitivity analysis using sparse polynomial chaos expansion. Water Air Soil Pollut. 223 (7). 4183–4197.

Feil B., Kucherenko S., Shah N., 2009.Comparison of montecarlo and quasimontecarlo sampling methods in high dimensional model representation. In: First International Conference on Advances in System Simulation. IEEE. New York. NY. pp. 12–17.

Fernàndez-Garcia D., Bolster D., Sanchez-Vila X., Tartakowsky D.M., 2012. A Bayesian approach to integrate temporal data into probabilistic risk analysis of monitored NAPL remediation. Adv. Water Res.. 36. 108–120.

Ghanem R.G., Spanos P.D., 1991. Stochastic Finite Elements: A Spectral Approach. Springer. N. Y.

Hillebrand O., Nodler K., Sauter M., Licha T., 2015. Multitracer experiment to evaluate the attenuation of selected organic micropollutants in a karst aquifer. Sci. Total Environ. ;506:338–343.

Jonker M.J., Svendsen C., Bedaux J.J.M., Bongers M., Kammenga J.E., 2005. Significance testing of synergistic/antagonistic, dose level–dependent, or dose ratio–dependent effects in mixture doseresponse analysis. Environ Toxicol Chem 24:2701–2713.

Le Maître O., Knio O., 2010. Spectral methods for uncertainty quantification. Scientific Computation. Springer. Heidelberg. Germany.

Maina F.Z., Guadagnini A., 2018. Uncertainty quantification and global sensitivity analysis of subsurface flow parameters to gravimetric variations during pumping tests in unconfined aquifers. Water Resour. Res. 54. 501–518

Seacat A.M., Thomford P.J., Hansen K.J. et al., 2002. Subchronic toxicity studies on perfluorooctanesulfonate potassium salt in Cynomolgus monkeys. Toxicol. Sci. 68, 249-264.

Stadler, J.C., 1986. One-year feeding study in dogs with carbendazim. Unpublished report from E.I. DuPont de Nemours and Co., Inc., Haskell Laboratory, Newark, Delaware, USA.

Sudret B., 2008. Global sensitivity analysis using polynomial chaos expansion. Reliab. Eng. Syst. Safe. 93 (7). 964–979.

Tartakovsky D.M., 2007. Probabilistic risk analysis in subsurface hydrology. Geophys. Res. Lett.. 34. L05404. doi:10.1029/2007GL029245.

Tixier C., Singer H.P., Canonica S., Müller S.R., 2002. Phototransfomation of ticlosan in surface waters: a relevant elimination process for this widely used biocide–laboratory studies, field measurements, and modeling. Environmental Science & Technology.;36:3482. doi: 10.1021/es025647t.

US EPA, 2014. Emerging Contaminants Perfluorooctane Sulfonate (PFOS) and Perfluorooctanoic Acid (PFOA). https://www.wqa.org/Portals/0/Government%20Relations/factsheet_contaminant_pfos_pfoa_march2014.pdf

Venkatesan P.S., Deecaraman M., Vijayalakshmi M., Sakthivelan S.M., 2014. Sub-acute toxicity studies of acetaminophen in Sprague Dawley rats. Biol Pharm Bull. 37, 1184-1190.

Xiu D., Karniakidis G.E., 2002. The Wiener-Askey polynomial chaos for stochastic differential equations. SIAM J. Sci. Comput. 24. 614-644.

Yu Y., Chu X., Pang G., Xiang Y., Fang H., 2009. Effects of repeated applications of fungicide carbendazim on its persistence and microbial community in soil. J. Environ. Sci. (China) 21, 179–85.

ANNEX I – Assessment of the quality of the surrogate model

Here, we assess the ability of gPCE described in Section 3.1 to approximate hydraulic heads at the $N_s = 34$ target points (i.e.. locations corresponding to springs). To this end, we randomly select $N_V = N_t/10$ sets of $\mathbf{Y}$ (validation sets) within the parameter space and calculate hydraulic head at location i (with $i = 1 \ldots N_s$) using the set of parameters j (with $j = 1 \ldots N_V$) through (i) the full model, $h_{i,j}$ (note these hydraulic head values have not been employed for the evaluation of the gPCE) and via, (ii) the gPCE-based surrogate model, $h_{gPCE,i,j}$, evaluated at order $w = 1$, 2, 3. Figures A1 depict scatterplots of $h_{gPCE,i,j}$ versus $h_{i,j}$ computed for the two conceptual models considered at all target points i and for all sets j. The Figure clearly shows a very good agreement between $h_{i,j}$ and $h_{gPCE,i,j}$ evaluated with $w = 3$.

We also computed the normalized root mean square error (NRMSE) between the full model and the gPCE approximation with $w = 3$. i.e.

$$NRMSE = \frac{1}{N_V}\sum_{j=1}^{N_V}\sqrt{\frac{1}{N_s}\sum_{i=1}^{N_s}\left(\frac{h_{gPCE,i,j} - h_{i,j}}{h_{i,j}}\right)^2}$$

obtaining, for $w = 3$, values of 0.009% and 0.027% for *CM* and *OC_A* respectively.

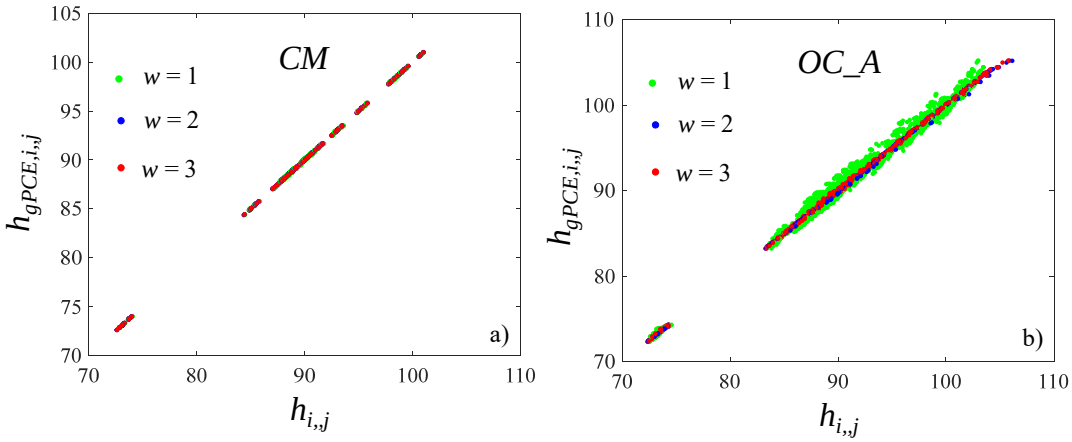

Figure A1. Scatterplots of hydraulic head values obtained through gPCE approximations versus full model counterparts for a) *CM* and b) *OC_A*.

ANNEX II – Wells and springs at the Cremona site

Name	Province	X_{GB}(m)	Y_{GB}(m)	Min-Max screen elevations (m)	Flow rate in the calibrated model (m^3/s)
Arzago	BG	1544191.49	5035759.62	20-80	0.53
Misano	CR	1549110.82	5035139.02	20-80	0.10
Capralba	CR	1550359.74	5031562.75	10-70	0.28
Sergnano	CR	1554018.61	5031106.58	10-70	0.05
Spino	CR	1538161.90	5026823.81	0-55	0.32

Table. A.1. Name and location of pumping wells considered in the analysis

X_{GB} (m)	Y_{GB} (m)	NAME	PROVINCE	TOWNS
1543450	5035830	ARZAGO D'ADDA_1 (Ar-1)	BG	ARZAGO D'ADDA
1544300	5036350	ARZAGO_2 (Ar-2)	BG	ARZAGO D'ADDA
1544250	5036580	ARZAGO_3 (Ar-3)	BG	ARZAGO D'ADDA
1542920	5037130	ARZAGO_4 (Ar-4)	BG	ARZAGO D'ADDA
1549924	5034089	BENZONA (Mi-2)	CR	CAPRALBA
1539752	5025488	BORLINA (Sp-4)	CR	SPINO D'ADDA
1548195	5032404	COLOMBERA (Ca-11)	CR	CAPRALBA
1548895	5032596	DEL CIMITERO EST (Ca-12)	CR	CAPRALBA
1550703	5033226	DELE LOTTE (Ca-17)	CR	CAPRALBA
1550848	5032569	DELLE CANNE (Ca-13)	CR	CAPRALBA
1550850	5032607	DELLE CANNE (Ca-15)	CR	CAPRALBA
1549363	5032086	FARINATE (Ca-9)	CR	CAPRALBA
1538457	5025675	FONTANELLA DI SPINO (Sp-5)	CR	SPINO D'ADDA
1553969	5033213	FONTANINE (Se-4)	CR	SERGNANO
1549590	5031487	FONTANONE DI CAPRALBA (Ca-2)	CR	CAPRALBA
1549620	5031535	FONTANONE DI CAPRALBA (Ca-3)	CR	CAPRALBA
1549627	5031671	FONTANONE DI CAPRALBA (Ca-5)	CR	CAPRALBA
1548282	5031947	MACCHERONE (Ca-6)	CR	CAPRALBA
1548347	5031953	MACCHERONE (Ca-7)	CR	CAPRALBA
1548412	5031960	MACCHERONE (Ca-8)	CR	CAPRALBA
1550039	5034878	MISANO (Mi-3)	BG	MISANO DI GERA D'ADDA
1549100	5034100	MISANO DI GERA D'ADDA (Mi-1)	BG	MISANO DI GERA D'ADDA
1549200	5035970	MISANO DI GERA D'ADDA_3 (Mi-4)	BG	MISANO DI GERA D'ADDA
1552782	5031477	MORGOLA (Se-3)	CR	SERGNANO
1537406	5025402	MOZZANICA (Sp-2)	CR	SPINO D'ADDA
1537423	5025438	MOZZANICA (Sp-3)	CR	SPINO D'ADDA
1548583	5031402	ORIOLA (Ca-1)	CR	CAPRALBA
1537456	5025385	PORTICO (Sp-1)	CR	SPINO D'ADDA
1548885	5032818	QUARANETINA (Ca-16)	CR	CAPRALBA
1548082	5032526	QUARANTA (Ca-10)	CR	CAPRALBA
1548889	5032662	QUARANTINA (Ca-14)	CR	CAPRALBA
1553417	5030465	SCHIAVA (Se-1)	CR	SERGNANO
1553424	5030361	SCHIAVA (Se-2)	CR	SERGNANO
1548332	5031632	SEREDEI (Ca-4)	CR	CAPRALBA

Table. A.2. Name and location of springs considered in the analysis.

ANNEX III – Statistics of optimal flow rates

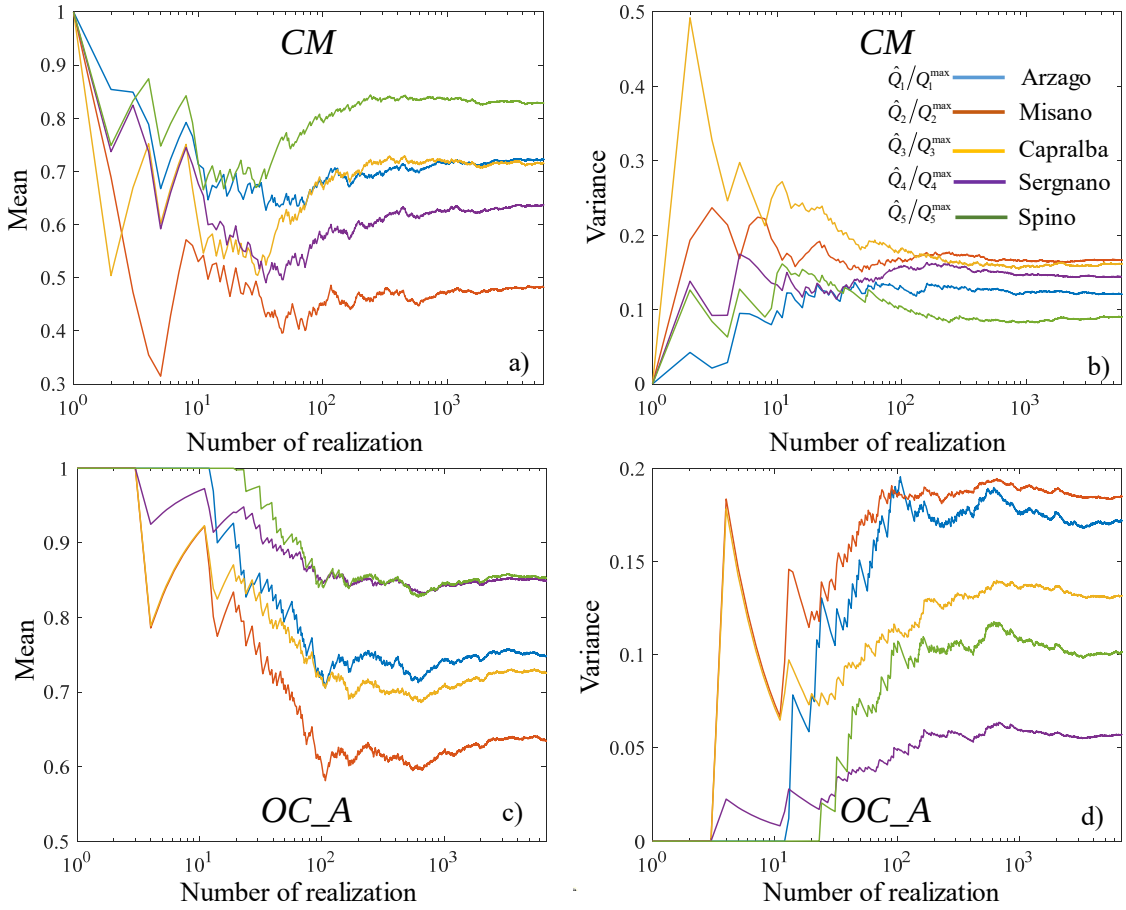

Figure A2. Mean and variance of optimal flow rates versus number of Monte Carlo realization for a-b) *CM* and c-d) *OC_A*.

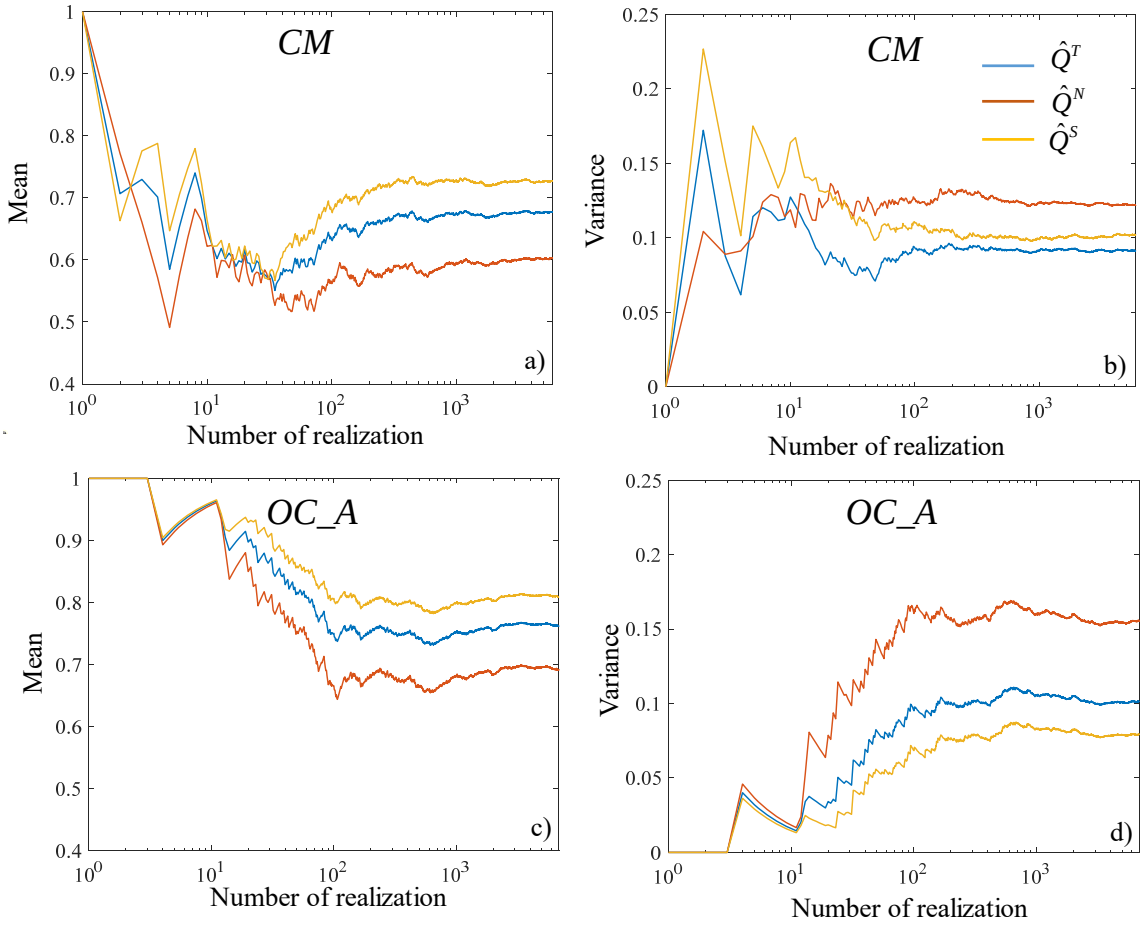

Figure A3. Mean and variance of optimal flow rates $\hat{Q}^T$, $\hat{Q}^N$ and $\hat{Q}^S$ versus number of Monte Carlo realization for a-b) *CM* and c-d) *OC_A*.